A Single-Molecule Bioelectronic Portable Array for Early Diagnosis of Pancreatic Cancer Precursors

Genco, Enrico; Modena, Francesco; Sarcina, Lucia; Björkström, Kim; Brunetti, Celestino; Caironi, Mario; Caputo, Mariapia; Demartis, Virginia Maria; Di Franco, Cinzia; Frusconi, Giulia; Haeberle, Lena; Larizza, Piero; Mancini, Maria Teresa; Österbacka, Ronald; Reeves, William; Scamarcio, Gaetano; Scandurra, Cecilia; Wheeler, May; Cantatore, Eugenio; Esposito, Irene; Macchia, Eleonora; Torricelli, Fabrizio; Viola, Fabrizio Antonio; Torsi, Luisa

Published in:
Advanced Materials

DOI:
10.1002/adma.202304102
https://doi.org/10.1002/adma.202304102

Published: 01/01/2023

Document Version
Final published version

Document License
CC BY

ADVANCED MATERIALS
www.advmat.de

A Single-Molecule Bioelectronic Portable Array for Early Diagnosis of Pancreatic Cancer Precursors

Enrico Genco, Francesco Modena, Lucia Sarcina, Kim Björkström, Celestino Brunetti, Mario Caironi, Mariapia Caputo, Virginia Maria Demartis, Cinzia Di Franco, Giulia Frusconi, Lena Haeberle, Piero Larizza, Maria Teresa Mancini, Ronald Österbacka, William Reeves, Gaetano Scamarcio, Cecilia Scandurra, May Wheeler, Eugenio Cantatore, Irene Esposito,* Eleonora Macchia,* Fabrizio Torricelli,* Fabrizio Antonio Viola,* and Luisa Torsi**

A cohort of 47 patients is screened for pancreatic cancer precursors with a portable 96-well bioelectronic sensing-array for single-molecule assay in cysts fluid and blood plasma, deployable at point-of-care (POC). Pancreatic cancer precursors are mucinous cysts diagnosed with a sensitivity of at most 80% by state-of-the-art cytopathological molecular analyses (e.g., $KRAS^{mut}$ DNA). Adding the simultaneous assay of proteins related to malignant transformation (e.g., MUC1 and CD55) is deemed essential to enhance diagnostic accuracy. The bioelectronic array proposed here, based on single-molecule-with-a-large-transistor (SiMoT) technology, can assay both nucleic acids and proteins at the single-molecule limit-of-identification (LOI) (1% of false-positives and false-negatives). It comprises an enzyme-linked immunosorbent assay (ELISA)-like 8 × 12-array organic-electronics disposable cartridge with an electrolyte-gated organic transistor sensor array, and a reusable reader, integrating a custom Si-IC chip, operating via software installed on a USB-connected smart device. The cartridge is complemented by a 3D-printed sensing gate cover plate. $KRAS^{mut}$, MUC1, and CD55 biomarkers either in plasma or cysts-fluid from 5 to 6 patients at a time, are multiplexed at single-molecule LOI in 1.5 h. The pancreatic cancer precursors are classified via a machine-learning analysis resulting in at least 96% diagnostic-sensitivity and 100% diagnostic-specificity. This preliminary study opens the way to POC liquid-biopsy-based early diagnosis of pancreatic-cancer precursors in plasma.

1. Introduction

Timely detection of a biomarker (or of a set of biomarkers) can endow a clinician with the attacker advantage over a progressive disease, enabling fast diagnosis, and effective therapeutic interventions contributing to creating a truly preventive and cost-effective healthcare system. Diagnostic protocols encompassing the assay of specific biomarkers of a disease (e.g., cancer, infection, neurodegenerative, cardiovascular, and autoimmune diseases, etc.) are, hence, gaining momentum.[1] To enable sensitive, convenient, non-invasive, and reliable early detections of markers, suitably engineered assay platforms are needed both in translational research and in the clinic.[2–4] Ideally, a biomarker-based diagnostic platform for screening purposes, should be able to: i) detect a single-molecule of each target biomarker in a reliably quantified volume of 0.1 mL to allow identifying the onset of a pathology; ii) deliver output results directly to the end-user with a short time-to-results; iii) be easy-to-operate and deployable at point-of-care (POC)

E. Genco, E. Cantatore
Department of Electrical Engineering
Eindhoven University of Technology
Eindhoven 5600 MB, The Netherlands
E-mail: e.cantatore@tue.nl

The ORCID identification number(s) for the author(s) of this article can be found under https://doi.org/10.1002/adma.202304102

[+]Present address: Dipartimento di Ingegneria Elettrica ed Elettronica, Università degli Studi di Cagliari, Via Marengo 3, Cagliari 09123, Italy

DOI: 10.1002/adma.202304102

F. Modena, M. Caironi, F. A. Viola[+]
Center for Nano Science and Technology
Istituto Italiano di Tecnologia
Via Rubattino 81, Milan 20134, Italy
E-mail: fabrizio.viola@iit.it

F. Modena
Dipartimento di Elettronica
Informazione e Bioingegneria
Politecnico di Milano
Piazza Leonardo da Vinci 32, Milan 20133, Italy

L. Sarcina, C. Scandurra, L. Torsi
Dipartimento di Chimica and Centre for Colloid and Surface Science
Università degli Studi di Bari Aldo Moro
Bari 20125, Italy
E-mail: luisa.torsi@uniba.it

sites (patient' house, but also doctor office, small rural hospitals in resource-limited-settings, pharmacy, where healthcare professionals can be present); iv) come in a small footprint with built-in real-time connectivity, being also robust; v) assay peripheral fluids such as blood, urine or saliva, being minimally to non-invasive; vi) being highly reliable by assuring an incidence of false-positive and false-negative random errors below 3–5%. These are some of the characteristics identified also in a REASSURED-type diagnostic[5] platform for POC screenings aiming at identifying a subset of asymptomatic individuals.

Proteins are considered an important complement to genetic markers not only in cancer but also in the early-diagnosis of cardiovascular diseases.[6,7] Thus, multiplexing (i.e., assaying a set of specific biomarkers simultaneously in the same sample) nucleic-acids as well as protein biomarkers, is deemed essential to improve diagnosis accuracy.[6–8] Moreover, ultrasensitive immunometric assays of protein markers are becoming crucial, a paradigmatic example being the neurofilament light protein single-molecule assay in cerebrospinal fluid for the early diagnosis of neurodegenerative syndromes.[9] Direct immunometric detection of pathogens (as opposed to the assay of their genetic components) is also significant, being a faster option as it generally requires no sample pretreatment. However, immunometric POC strip-tests notoriously lack reliability being plagued by a high-incidence of false negatives (low diagnostic sensitivity).[10]

Traditional immunometric methods (e.g., enzyme-linked immunosorbent assay (ELISA))[11–13] operating at limit-of-detections (LODs)[14] of picomolar (10^{-12} mol L^{-1}, pM, 10^8 markers in 0.1 mL),[13] are not sufficiently sensitive to detect the few biomarkers that enable to predict diseases' onset, well before symptoms appear. This holds true in liquid biopsy too as in peripheral biofluids (as opposed to tumor-tissues' juices, interstitial fluids, etc.) the concentration of biomarkers is extremely low.

The clinical relevance of biomarkers was unveiled by polymerase-chain-reaction (PCR)[15] based platforms, presently the gold-standard in molecular assays, that can reliably detect low abundance nucleic-acid (DNA, RNA, etc.) markers in biofluids. Highly specific detection is actuated via the biomarker pairing to a complementary nucleotide probe, while sequencing of an unknown genome (e.g., of a tumor cell) is possible with pH-sensitive CMOS technologies such as next-Ggeneration sequencing (NGS).[16] The PCR-amplification of the targeted marker is key to reaching the unprecedented sensitivity of one nucleic-acid copy in 0.1 mL, namely a LOD of 10^{-20} M or 10 zM. Paramagnetic-beads-based ultrasensitive immunoassay technologies, e.g., single-molecule array (SIMOA),[17,18] targeting antigens/proteins with capturing antibodies, are now commercially available too. ELISA's limitation is overcome by restraining individual enzymes and their fluorogenic substrate into femtoliter-sized wells. This enables LODs in the sub-femtomolar regime down to 220 zM (10 to 10^5 molecules in 0.1 mL).[18] The SIMOA planar technology (SP-X Imaging and Analysis System),[19,20] which is faster and more practical, operates, however, at higher LODs.[21] CRISPR-Cas[22] is an emerging ultrasensitive technology also aiming at advanced molecular detections[23–25] of different markers, ranging from nucleic-acids to proteins, but the latter ones are detected in the nM regime.[26] While these approaches can be, generally, extremely sensitive and specific, they require bench-top apparatuses and do not enable the detection of single-molecule of both protein and nucleic acid markers simultaneously in the same sample and with the same platform.

The single-molecule-with-a-large-transistor (SiMoT)[27,28] platform, developed so far only as a single-sensor,[29] is an handheld technology,[30] which reliably detects a single-marker of a protein or of a nucleic-acid[31,32] in a 0.1 mL droplet of a biofluid. The SiMoT single-sensor technology has been validated as a multipurpose platform successfully assaying the following biomarkers and pathogens: Immunoglobulin M (IgM),[33] IgG,[27] C-Reactive Protein (CRP),[34] p24 protein of the HIV-1 virus capsid (p24-HIV-1),[35] Spike1 (S1),[30] Mucin 1 (MUC1),[31] Interleukin 6 (IL-6),[36] $KRAS^{mut}$,[31] microRNA,[32] COVID-19,[30,37] *Xylella fastidiosa*.[38] They are all detected at the single-entity LOD level in physiological phosphate buffer saline (PBS) solution, saliva, serum, whole blood, swab or olive sap. The SiMoT single-sensor can also operate at the 10 zM limit-of-identification (LOI) ensuring a confidence level >99%, i.e., less than 1% of false-positives and false-negatives.[14] The assay is qualitative (yes/no-type with the threshold at the LOI), so in a POC mass-screening a SiMoT test can reliably assess if a droplet of saliva or plasma contains or not at least one marker or one pathogen. This is done in less than an hour and with minimal invasiveness. SiMoT relies on bioelectronic (both electrolyte-gated[33] and electrochemical[37,39]) organic field-effect transistors,[40–42] whose millimeter-wide gate is biofunctionalized with a layer of highly packed (10^4 μm^{-2}) antibodies or probes that can bind, in 10 min, a single antibody or probe.[43] The sensor detects via the capacitive coupling

K. Björkström, R. Österbacka, E. Macchia
The Faculty of Science and Engineering
Åbo Akademi University
Turku 20500, Finland
E-mail: eleonora.macchia@uniba.it

C. Brunetti, P. Larizza, M. T. Mancini
Masmec Biomed – Masmec SpA division
Modugno (BA) 70026, Italy

M. Caputo, E. Macchia
Dipartimento di Farmacia-Scienze del Farmaco
Università degli Studi di Bari "Aldo Moro"
Bari 70125, Italy

V. M. Demartis, G. Frusconi, F. Torricelli
Dipartimento Ingegneria dell'Informazione
Università degli Studi di Brescia
Brescia 25123, Italy
E-mail: fabrizio.torricelli@unibs.it

C. Di Franco, G. Scamarcio
CNR IFN
Bari 70126, Italy

L. Haeberle, I. Esposito
Institute of Pathology
Heinrich-Heine University and University Hospital of Düsseldorf
40225 Duesseldorf, Germany
E-mail: irene.esposito@med.uni-duesseldorf.de

W. Reeves, M. Wheeler
FlexEnable Technology Ltd
Cambridge CB4 0FX, UK

G. Scamarcio
Dipartimento Interateneo di Fisica
Università degli Studi di Bari Aldo Moro
Bari 70125, Italy

of the gate electrode with the channel of an electrolyte-gated transistor.[28] This enables to measure a change in the current flowing in the transistor when the electrochemical potential of the gate changes because of the affinity binding. More specifically, SiMoT detects a single biomarker on a capturing surface that contains trillions of biorecognition elements. This presents a challenge as the signals from individual binding events are expected to be much lower than the background noise.[27,43,44] To address this, an amplification mechanism, which involves a domino-like propagation of an electrostatic change triggered by the affinity binding at a single capturing antibody, has been proposed. This change ultimately affects numerous other antibodies, amplifying the signal. Such a mechanism is based on the propagation of an electrostatic change occurring on a single capturing antibody among those capturing biorecognition elements that are densely packed on the gate surface. Experimental evidence supporting this mechanism was obtained by means of the Kelvin probe force microscopy, which showed that the binding of 10 proteins to an equal number of anti-IgMs caused a surface potential shift in 10^8 anti-IgMs that were packed on a 90×90 μm^2 wide electrode.[44]

Pancreatic cancer is a highly aggressive form of cancer and is responsible for the third-highest number of cancer-related deaths in Western nations.[45] Only ≈20% of patients can undergo surgery to potentially cure cancer,[46] and the survival rate beyond five years is currently only 9%.[47] The limited number of risk factors that can be modified further complicates treatment options.[48] Though biomarkers for pancreatic cancer early detection are not available yet, intraductal and cystic lesions are widely recognized as precursors.[49,50] Among other cystic lesions that are rarer or can be only detected microscopically, the mucin-producing cystic neoplasms or mucinous cysts (e.g., intraductal papillary mucinous neoplasms and mucinous cystic neoplasms),[50,51] are the most common. While intense activity for the identification of suitable biomarkers of the mucinous cysts is ongoing,[52,53] nowadays they are still detected incidentally in imaging studies performed on individuals without pancreas-specific symptomatology. Once a pancreatic lesion is diagnosed it needs to be sorted into benign (nonmucinous, or pseudocysts), probably malignant (low- and high-grade mucinous cysts) or frankly malignant (cancer) to adequately treat the patient that can be discharged, enter a follow-up protocol, or undergo surgical resection. The identification of the high-grade mucinous lesions is most critical as they are those at high-risk of transformation into invasive cancer.[54] According to recent guidelines, ultrasonography with puncture of the cyst for histo-cytopathological analysis can support a preoperative diagnosis, which in turn directs therapy.[55] However, standard cytopathology diagnostic sensitivity (true positive rate) is not sufficiently high, and ancillary NGS molecular tests based on cell-free DNA from the cyst fluid or tissue analysis, are usually applied.[52–54,56] To this end, in cyst fluids from low-grade and high-grade mucinous cysts, characteristic pathogenic mutations of KRAS, GNAS and/or TP53 genes among others, are considered suitable markers.[57,58] NGS-based blood plasma analysis is currently being investigated for diagnosis and monitoring of pancreatic cancer; however, no reliable assay for the detection of pancreatic cancer precursors is available yet.[59] The analysis of pancreatic cyst fluids by NGS improves the sensitivity of cytopathology in the identification in a preoperative setting of mucinous cysts, from 54% to 92%, and the sensitivity of the detection of high-grade mucinous cysts from 50% to 71%.[54] Although this approach increases sensitivity according to numerous studies, still performance is not fully satisfactory and the whole procedure takes 3–10 days. To improve the performance level, the ultrasensitive simultaneous detection of oncoproteins such as Mucin 1 (MUC1),[60–62] and Complement-decay-accelerating factor (CD55),[63] is considered of very high relevance.

To improve the diagnosis reliability of pancreatic cancer precursors, the SiMoT technology is upscaled into a multiplexing 96-array prototype at Technology-Readiness-Level (TRL) 5 in the framework of a 4-year collaborative EU project: "Single-molecule bioelectronic smart system array for clinical testing—SiMBiT."[64] The SiMBiT platform comprises a disposable cartridge and a reusable reader. The cartridge integrates printed electrolyte-gated organic field-effect transistors (EGOFETs) sensors, arranged in a disposable 8×12 ELISA-like array, which is complemented by a 3D-printed lid of sensing gates and by multiplexing electronics fabricated with organic thin-film transistors (OTFTs). The sensing gates are biofunctionalized either with capturing antibodies or probes. The reader integrates a custom-designed Si-IC chip that operates via dedicated software installed in a USB-connected smart device. The prototype is engaged in a preclinical trial involving the assay of 47 unselected patients' cyst fluids (35 patients) and blood plasma (12 patients). To this end, single-molecule assays of proteins (MUC1 and CD55) and nucleic-acid (KRAS mutations, KRAS^{mut}) biomarkers were performed simultaneously and benchmarked against state-of-the-art histo-cytopathology complemented by NGS. A machine-learning algorithm is engaged to reliably classify the samples analyzed with the SiMBiT prototype as belonging to a potentially nonmucinous or low-grade cyst, or from a high-grade one. A *k*-nearest neighbor (*k*-NN) classifier is instructed on a training set comprising 37 samples. The classifier predictive performance is evaluated on an external test set, consisting of 10 samples assayed in double-blinded, not engaged in the algorithm training stage. The SiMBiT technology is proven capable of correctly predicting all the samples of the external test set, as confirmed by the diagnosis formulated through histo-cytopathology complemented by NGS molecular analysis. The results of a benchmarked cost and time analysis show that SiMBiT is also fast (time-to-results in 1.5 h) and cost-effective (<100 €), for the multiplexing analysis of 5–6 patients. These remarkable results, though based on a limited number of patients, open the route to the possibility of performing in the future, a completely new minimally invasive POC liquid-biopsy screening for early diagnosis of pancreatic cancer and hold the potential to save millions of lives.

2. Results and Discussion

2.1. The 96-Well Bioelectronic Prototype

The overall structure of the SiMBiT portable prototype developed at TRL5, is shown in **Figure 1**. It consists of a disposable cartridge comprising 96 bioelectronic sensors, with the same form factor of a standard 8×12 ELISA plate, and a reusable reader that operates via an USB connection to a standard smart device

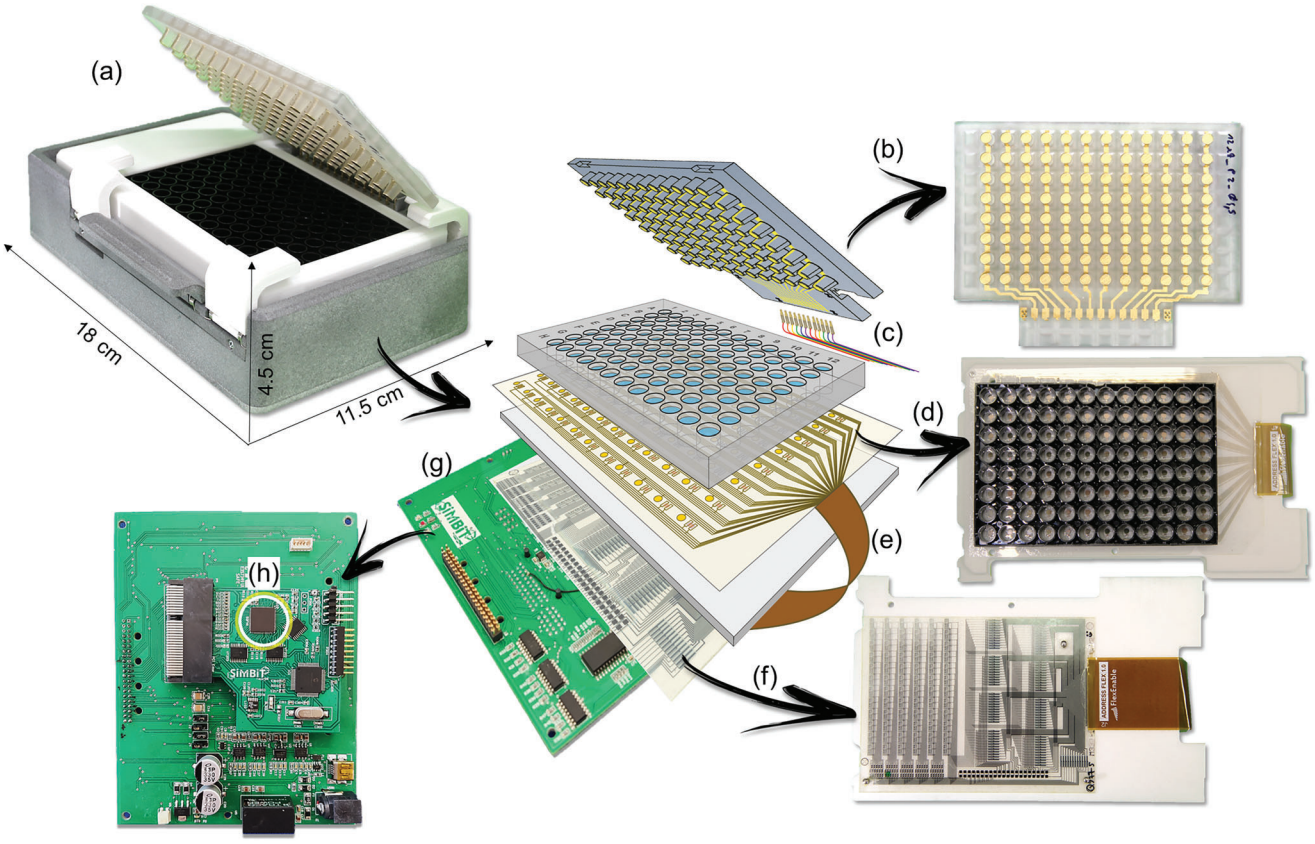

Figure 1. a) Picture of the small footprint (18 cm × 11.5 cm × 4.5 cm) SiMBiT bioelectronic platform. The disassembled system, shown on the right, comprises, from top to bottom, the following elements: b) a 3D-printed array of biofunctionalized sensing gates covering the ELISA plate, c) spring-loaded pins connectors, d) an array of the EGOFETs on poly(ethylene 2,6-naphthalate) (PEN)-foil glued on a bottomless ELISA-plate, e) flat cable connecting the bioelectronics array to the f) multiplexing electronics based on a unipolar OTFT-based technology (FlexEnable Technology), g) a printed circuit board (PCB), integrating h) a custom Si-IC chip.

(computer, tablet, etc.). In Figure 1a a picture of the complete device is shown, while the disassembled system is featured in Figures 1b–h, evidencing all components, namely: i) the 3D-printed array of biofunctionalized sensing-gates (SG) designed to fit the ELISA plate as a cover; it is endowed with trunked conical shape pillars (Figure 1b) that protrude into the wells to get in contact with the deionized water filling them; ii) spring-loaded pins (Figure 1c) placed along-side the prototype connecting the 3D-printed array; iii) a flexible EGOFET array fabricated on a poly(ethylene 2,6-naphthalate) (PEN)-foil, on top of which a bottomless ELISA black plate is glued (Figure 1d); iv) the flat cable (Figure 1e) connecting the EGOFET sensor array to the multiplexing electronics; v) the unipolar OTFT-based multiplexing electronics produced by FlexEnable Technology (Figure 1f); vi) a printed circuit board (PCB) (Figure 1g) integrating a custom-designed Si-IC chip fabricated in 65 nm CMOS technology (Figure 1h).

The PCB and the Si-IC form the reusable electronic reader, which provides all modules with the required signals and sends the data to the software via a USB port. The disposable cartridge is composed of the EGOFET array, the 3D-sensing gate plate, and the OTFT multiplexing electronics. The 96 EGOFET array (**Figure 2**a) is manufactured on a PEN substrate. Each EGOFET comprises a coplanar lateral gate (LG) which serves as a monitoring gate for the stability of the device,[65] along with the source (S) and drain (D) interdigitated gold electrodes covered by the inkjet printed organic semiconductor, namely poly(3-hexylthiophene) (P3HT), while the gold traces are covered with an inkjet printed insulating biocompatible SU8 layer (Figure 2b). All gates present in each column of the array are shorted together: This is achieved by inkjet printing a conductive silver ink, bridging the SU8 insulator, as shown in Figure 2a. In Figure 2c the equivalent circuit involving the LG is shown. A bottomless black ELISA plate is glued around each EGOFET using a patterned medical-grade double-sided adhesive foil, allowing the dispensing of 300 µL of deionized water (HPLC grade) serving as the electrolyte, which couples the gates (the lateral or the 3D sensing ones) to the channel via electrical double layers (EDL).[65] Using the same adhesive, the EGOFET array is attached to a thick plastic substrate. The SiMBiT disposable cartridge is completed by the OTFT-based multiplexing electronics connected to the EGOFET array via a flat cable, altogether forming the e-ELISA plate. While the 3D sensing gate plate is a one-time-use-only disposable part, the e-ELISA plate was used for several sensing runs (≈32 sensing runs, for a total of 192 patients' samples assessments), before being disposed of.

The SiMBiT prototype is completed by the reusable electronic reader connected to the e-ELISA plate. This comprises the

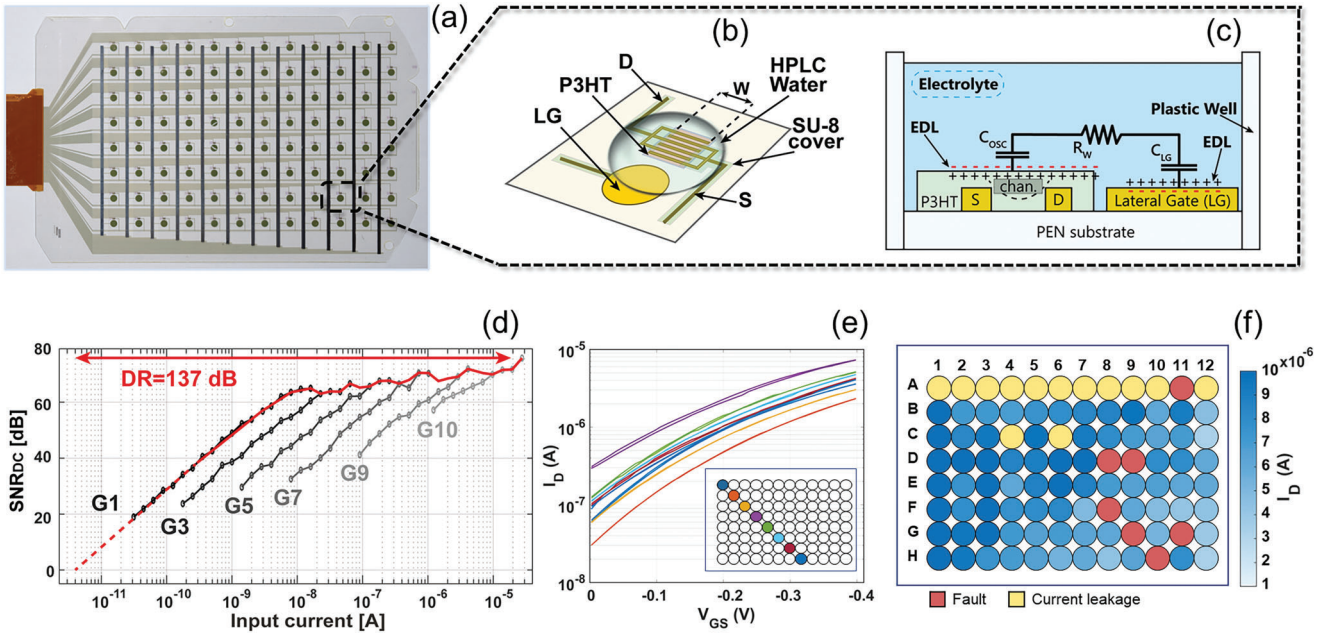

Figure 2. a) Picture of the Eelectrolyte-gated organic field-effect transistor (EGOFET) flexible array. b) Schematic of the EGOFET structure with the lateral-gate and c) its equivalent circuit. d) Measured signal-to-noise-ratio (SNR) and dynamic range (DR) of the silicon integrated circuit (Si-IC): Gain 1 to Gain 10 (G1–G10) are the gain settings of the active feedback programmable gain transimpedance amplifier (AFPG-TIA). e) Typical transfer curves of EGOFETs measured from devices positioned in different points of the array (see inset). f) Uniformity of the EGOFET array maximum output currents, highlighting faulty devices.

custom Si-IC chip that performs three main functions: i) generation of the biasing voltages and acquisition of the 96 EGOFETs currents, ii) control of the measurement process, and iii) communication via USB to a base station. The chip is manufactured in a commercial CMOS 65 nm technology[66] and acts as the interface between the e-ELISA and the ad hoc developed software installed in the main computing unit. A digital-to-analog converter (DAC) embedded in the Si-IC is used to supply bias voltages to the EGOFET lateral and sensing gate contacts, while the drain and source are kept at a stable voltage difference. The EGOFET drain current measured in this biasing condition is processed by a multiplexed current-sensitive analog front-end (AFE). Together with an additional dedicated analog-to-digital converter (ADC), this circuit translates the current signals coming from a column of 8 EGOFETs to digital data. As EGOFETs exhibit an exceptionally high capacitance and a wide output current range is to be processed, the AFE should offer a dynamic range (DR) exceeding 120 dB.[66] A novel active-feedback programmable-gain transimpedance amplifier (AFPG-TIA) has been designed to meet all these requirements.[66]

The multiplexing electronics connects one column of EGOFETs at a time to the reader, to measure in parallel each of the eight sensors drain currents, and keeps all the other EGOFETs disconnected (Section S1 and Figure S1, Supporting Information). This operation is repeated twelve times to sequentially read all columns. The electronic reader also addresses the 3D-sensing gates. To this end, the gold-coated pillars are connected column-wise, automatically addressing only the column of 3D gates whose EGOFETs currents are being read. While addressing the 3D-sensing gate array, the lateral gate contacts are disconnected. Conversely, when the 3D gate array is not in use (e.g., during the incubations, vide infra), the lateral gates are biased to independently control the EGOFETs current stability.

2.1.1. SiMBiT System Electrical Characterization

In Figure 2d the measured signal-to-noise-ratio (SNR) and dynamic range (DR) of the Si-IC (Section S2 and Figure S2, Supporting Information) are shown, over the whole drain current range measured in an EGOFET for a varying LG bias. Due to the very large capacitance associated with an electrolyte EDL, an EGOFET drain current typically spans from tens of nA to tens of μA. An AFE with an extended dynamic range is hence needed to record any current with an error lower than 1‰. In Figure 2e the EGOFET transfer characteristics (I_D vs V_{GS} at $V_D = -0.4$ V) were measured sweeping the LG of 8 different devices (one for each row in different columns), proving an acceptable uniformity of the measured values (device-to-device variation within ±60%). In Figure 2f the maximum current recorded for each of the 96 EGOFETs of a SiMBiT array is displayed, proving that only 7 devices were faulty (i.e., short-circuited) while 14 were leaky and not suitable for biosensing. Generally, the arrays reached an overall yield of about 80%. Such yield is intended for improvement as the manufacturing moves from research to industrial environment. The current drain current variability shown in Figure 2e, and the possible occurrence of faulty devices reported in Figure 2f were foreseen in the system design phase. The former issue is effectively solved by the sensing protocol (Section 2.2), which extracts the information on the binding from the normalized difference of the drain current read before and after the incubation phase and is thus insensitive to the absolute value of the drain current.

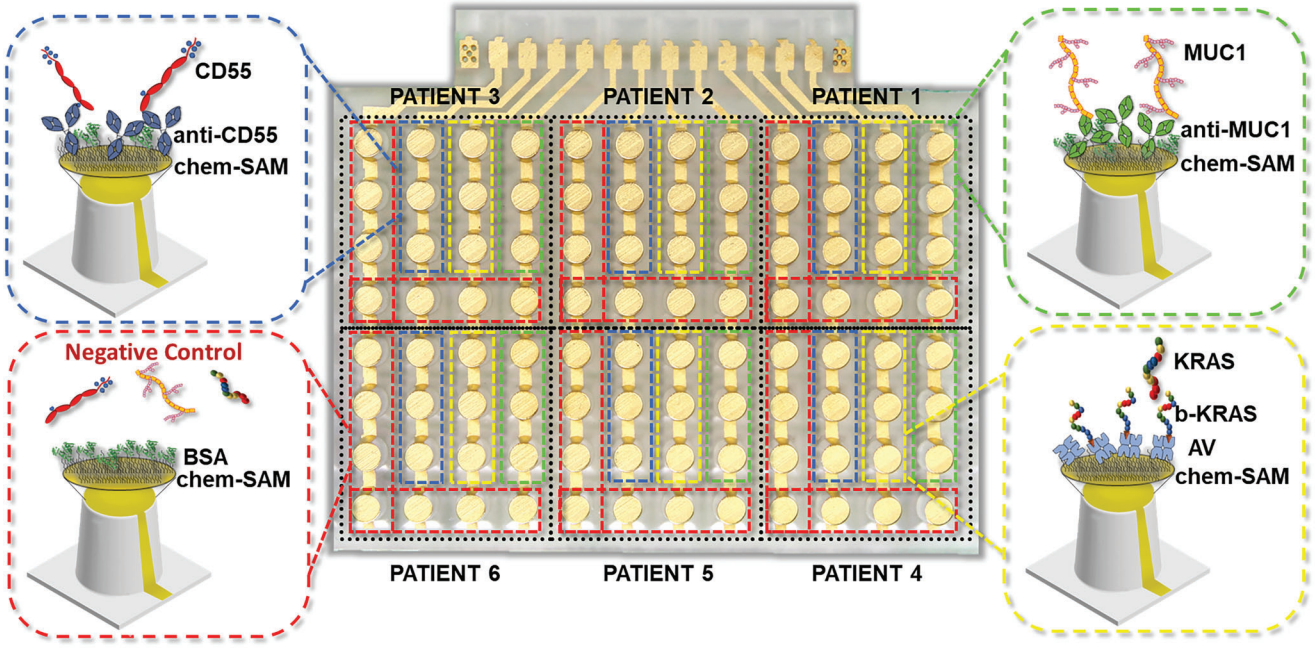

Figure 3. Top view of the 3D printed sensing gate plate showing the gold-plated circular areas and the paths to the contact pads. The plate is divided into 6 areas each one assigned to the sensing of the fluid of one patient. The colour codes identify the gates (in triplicates) that are biofunctionalized with the capturing antibodies against MUC1 and CD55 or the probes to bind $KRAS^{mut}$. Each patient fluid is also exposed to 7 gates that are biofunctionalized with BSA for the negative-control experiments.

The effect of faulty sensors is mitigated by the redundancy of the measurements, and by choosing working sensors instead of the faulty devices.

2.1.2. 3D-Printed Array of the Sensing Gates

The fabrication of the 3D array of the sensing gates was performed by a 3D printing stereolithography (Section S3 and Figure S3–S6, Supporting Information). It features 96 truncated cones that fit a standard ELISA plate. The roughness was reduced by depositing a 2 µm thick layer of Parylene-C. Gold was deposited by e-beam evaporation on the planarized 3D gate plate structure, defining the circular gate area on top of the truncated pillars and the paths to the pads' contacts. The gold thickness is about 150 nm. The gates are biofunctionalized with a specific recognition element, covalently bound to the gold gate, which highly selectively binds a given marker.

The biofunctionalization process comprises a thiol-based chemical self-assembled-monolayer (chem-SAM) to which the capturing antibodies for MUC1 and CD55, anti-MUC1 (green-box, **Figure 3**), and anti-CD55 (blue-box, Figure 3), are conjugated. For the $KRAS^{mut}$, avidin (AV) is conjugated to the chem-SAM and a biotinylated $KRAS^{mut}$ complementary strand (b-$KRAS^{mut}$) serves as the probe (yellow-box, Figure 3). The negative control experiments are carried out on gates biofunctionalized with the non-binding bovine serum albumin (BSA, red-box, Figure 3). The biofunctionalization results in the covalent binding on the millimeter-wide sensing gate surface, of trillions of capturing elements (Section S4 and Figure S7, Supporting Information).[27,67] The plate is divided into 6 subsets of 16 gates, and each subset is exposed to the fluids (cysts or plasma) of a given patient. For each patient, three replicates for each of the three biomarkers are measured, along with 7 control experiments. To comply with the less than 100% yield of the SiMBiT array, 5 patients run was also carried out.

2.2. Multiplexing Sensing Protocol

The sensing encompasses a few very easy steps shown in **Figure 4**. The protocol starts with the properly biofunctionalized array of gates that are incubated for 10 min in a phosphate buffer saline (PBS, ionic strength = 163×10^{-3} M and pH = 7.4) solution serving as reference fluid. This is performed by immersing the biofunctionalized 3D sensing gate array into a standard ELISA plate where all the wells are filled with the PBS solution (Figure 4a). Meanwhile, the already stabilized array of EGOFETs (see the Experimental Section for the stabilization protocol) is operated in deionized water by measuring 20 transfer characteristics (I_D vs V_{GS}) sweeping the lateral gate (LG), serving as reference. This is referred to as "cycling" and is carried out in each of the 96 wells, addressing one column at a time. As the devices are stable, the 20 curves will almost completely overlap as shown in Figure 4b. The 3D sensing gate plate is washed in deionized water and transferred into the well of the EGOFET array covering the plate as a lid; here the cycling is carried out again, biasing the 3D sensing gates. While each "cycling" takes 2.5 min, the whole process takes overall 30 min to address all 12 columns. The resulting curves are the baseline I_0, again measured in each well. Typically measured curves (20 almost overlapping traces) are shown as blue lines in Figure 4c. The

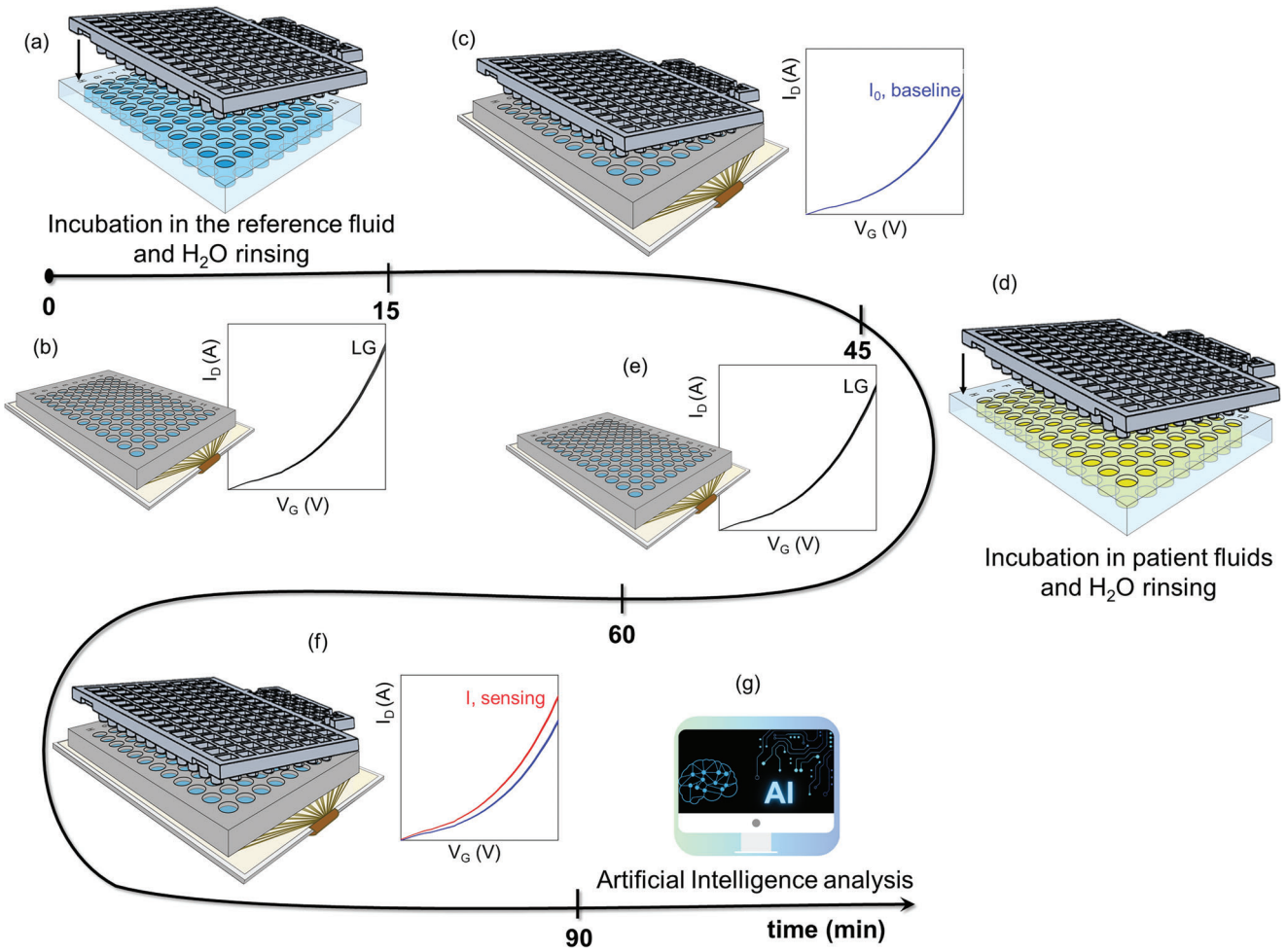

Figure 4. The steps of the multiplexing sensing protocol (see text for details and Video S1 in Supporting Information).

3D-sensing gates plate is now transferred into a standard ELISA plate filled with the fluids of 5–6 patients (according to the 4 × 4 subsets illustrated in Figure 3) and incubated for 10 min (Figure 4d). Meanwhile, a second run of transfer characteristics is measured with the lateral gate; at this stage too, the 20 curves measured are hardly distinguishable and are also very similar to those measured during the step in Figure 4b, proving the high stability of the EGOFET array. If at this stage a given EGOFET shows a shift in current larger than 10% (as compared to what is measured at the previous check shown in Figure 4b), the sensing from that well is discarded. As a last step, the 3D sensing array is removed from the patients' fluids, is washed in deionized water, and is positioned on the EGOFET array to undergo the cycling of 20 curves, shown in red in Figure 4f, along with the baseline traces in blue.

The shift of the current signal is readily apparent and the whole process to assess 5–6 patients against three markers takes 90 min. The data are now transferred to a computer via a USB port and an AI-based classifier performs reliable (false-positive and false-negative < 1%) discriminant classification of high- and low-grade, and nonmucinous cysts. A video of the whole sensing process is provided (Movie S1, Supporting Information).

2.3. The Clinical Assay on Pancreatic Cancer Patients

2.3.1. SiMBiT Single Marker Detection at 10 zM in 0.1 mL

The sensing protocol illustrated in Figure 4 is applied to the simultaneous sensing of MUC1, CD55, and $KRAS^{mut}$ at the single-molecule level. To this end, PBS is spiked with the markers at 10 zM (1 ± 1 molecule in 0.1 mL). The gates are biofunctionalized according to the 4 × 4 subset structure defined in Figure 3, which foresees triplicates for the sensing of each marker and 7 negative control experiments. The results of the negative control experiments are shown in **Figure 5**a. In these experiments, the gate, biofunctionalized with the nonbinding BSA, is exposed to PBS solutions added with all three markers (KRAS, MUC1, and CD55) at a very high concentration of 10×10^{-9} M (10^{12} molecules in 0.1 mL), namely 12 orders of magnitude higher than those in the single-molecule experiments. Even at these much higher concentrations, the BSA noncapturing element is shown not to bind any of the markers. The central panel in Figure 5a shows the sensing currents I (20 cycles, red curves) and the baseline (20 cycles, blue curves) I_0, taken after incubation in the reference fluid, proving that, in the

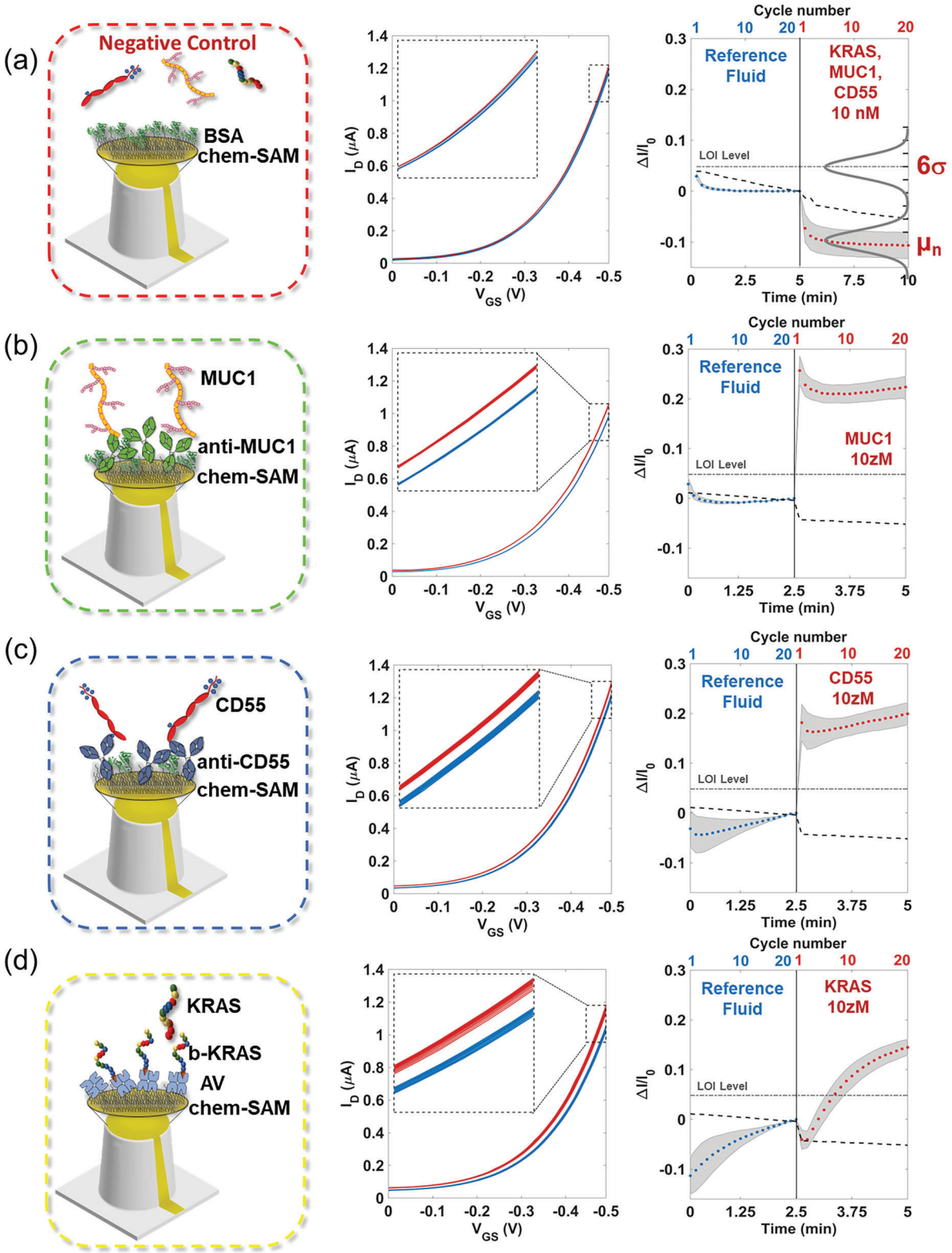

Figure 5. a–d) SiMBiT sensing measurements according to the protocol described in Figure 4, carried out in: a) PBS added with 1×10^{-9} M of MUC1, CD55, and KRAS^{mut} (negative control experiments); or b–d) in PBS added with MUC1 (b), CD55 (c), or KRAS^{mut} (d) at 10 zM. The leftmost panels feature the schematics of the gate pillars illustrating the chem-SAM, the capturing recognition elements (anti-MUC1, anti-CD55, b-BRAS), and their affinity ligands; the negative control experiments involve a gate functionalized with BSA that is exposed to all the three markers (KRAS, MUC1, and CD55) at a concentration of 10×10^{-9} M. The central panels show the sensing

absence of an affinity binding, no significant difference is recorded between the baseline current and sensing signal. On the rightmost panel of Figure 5a the relative current shift upon sensing, $\Delta I/I_0 = (I - I_0)/I_0$ (currents measured at $V_{GS} = -0.5$ V and $V_D = -0.4$ V vs time during each cycle), is shown. Here the red curve is the average of the currents measured for the 7 control experiments, while the gray shaded area is the data dispersion over 1σ (see also Section S5 and Figure S8, Supporting Information). The first 20 cycles, measured in water after incubation in PBS (first 2.5 min) are characterized by a very low data dispersion. A slightly larger noise is seen when the BSA gate is cycled (subsequent 2.5 min) after incubation in the PBS solution added with the 3×10^{12} biomolecules (proteins and DNA), possibly because the markers, although not binding to the gate, are anyhow bumping onto the gate surface slightly changing its electrochemical potential. The random error Gaussian distribution is featured in the panel (rightmost in Figure 5a), around the average value μ_n, as a gray line. The measured noise level in PBS added with the markers is used to evaluate the LOI as the average of the negative control experiment noise level, μ_n, plus 6 times its standard deviation, σ. The Gaussian distribution of the random error at the LOI is also shown in the figure as a dark gray line.

The dashed black curve is the relative current shift occurring at the lateral gate, measured before and after the sensing. In Figure 5b the MUC1 protein is detected at the single molecule level. The central panel shows the transfer curves of the baseline (measured after incubation in PBS) and the signal (after incubation in MUC1, 10 zM in PBS), while the rightmost panel shows the dynamic of the $\Delta I/I_0$. As it is apparent, a clear signal change, well beyond the LOI, is seen upon the sensing of one MUC1 protein. For CD55 (Figure 5c) very similar data were measured and single molecule sensing was proven too. A slightly slower $\Delta I/I_0$ dynamic (rightmost panel in Figure 5d) is seen for $KRAS^{mut}$ but the final value of the $\Delta I/I_0$ leaves no doubt that the signal is beyond the LOI level also in this case. In all cases, the lateral gate current relative change (dotted black line) is always below a few percent of relative variation (proving the device stability) and is also always below the LOI. These data clearly show that the SiMBiT technology can discriminate, in a yes/no-type fashion with the threshold at the LOI (confidence level better than 99%), if in a droplet of 0.1 mL of a physiological relevant fluid (e.g., PBS), there is or there is not at least one single molecule of a given marker. Moreover, it was already demonstrated that an incubation of 10 min is enough for the single-molecule binding to occur at the wide gate interface.[43]

2.3.2. Preclinical Trial

SiMBiT Analysis of 47 Patients' Fluids: The protocol illustrated in Figure 4 is further used to assay either the blood plasma or the cysts fluids of 47 patients. Typical measured data are shown in **Figure 6**. The schematics of the gate pillars illustrating the chem-SAM, the capturing recognition elements (anti-MUC1, b-$KRAS^{mut}$, anti-CD55, and BSA), and their affinity ligands, are featured in Figure 6a. In Figure 6b the typical current outputs for a plasma sample showing evidence of belonging to a high-grade mucinous cyst are featured for all three markers (from left to right: MUC1, $KRAS^{mut}$, and CD55), before and after incubation into the reference fluid and in the plasma.

The rightmost panel shows the output for the negative-control experiments, along with the relevant Gaussian distributions of the random error at the average level of the noise, μ_n, and at the LOI. This level is then shown also in the other 3 panels as a dashed-dotted dark-gray line. In Figure 6c the same data is presented for an assay in cysts fluid. In Figure 6d,e, the same curves are presented for the analysis of plasma or cysts fluids belonging to cysts being potentially low-grade (in fact showing no evidence of being high-grade in the sampled part of the cyst) and potentially nonmucinous (no evidence of being mucinous). The patients' status was assessed by state-of-the-art diagnosis based on demographic information, clinical/radiological data, cytology/biopsy, and NGS analysis of cell-free DNA obtained from cyst fluids, and, where available, NGS analysis of tissue samples after resection.

From the sensing data three features, *F1*, *F2*, and *F3* described in the Experimental Section, are extracted. *F1* accounts for the signal relative change as compared to the baseline, *F2* considers the slope of the current drift during cycling, *F3* is the off/on (0,1) characteristic with respect to the LOI (Section S5, Supporting Information). These indicators are taken as the characteristic elements of each sensing assay, serving as features in the artificial intelligence (AI) analysis. A table of all the AI feature values for the whole set of 47 patients is given in the "iMBiT Machine-Learning-Based Discriminant Classifier" part of the Experimental Section.

Multivariate Data Processing: An exploratory multivariate data processing based on principal component analysis (PCA) was undertaken to analyze the whole SiMBiT data set. PCA provides, for all three markers, an orthogonal set of principal components (PCs) described as a linear combination of each feature *F1*, *F2*, and *F3*), weighted by the eigenvalues of the loading matrix. The scores are the overall summed value for each PC. The details of the PCA analysis are provided in Section S5 (Supporting Information) (Figure S9a, Supporting Information) where it is demonstrated that the first two PCs (PC1 and PC2) suitably describe the whole data set, encompassing 9 features for each patient, i.e., 3 features for each of the 3 markers. The whole data set was divided into a training set of 37 samples and an external test set of 10 patients assayed in double blinded. The PCA was performed on the training set spotting no outlier

current I (red curves) and the baseline I_0 (blue curves) during the cycling involving the measurement of 20 transfer characteristic curves (I_D vs V_{GS} in the 0 to −0.5 V range at fixed $V_D = -0.4$ V measured in deionized water). The rightmost panels give the current relative change $(I - I_0)/I_0 = \Delta I/I_0$ vs cycles (top *x*-axis) and time (bottom *x*-axis). The current is measured in deionized water and the $\Delta I/I_0$ data-points are taken at $V_{GS} = -0.5$ V and $V_D = -0.4$ V, one for each of the 20 cycles. The whole cycling takes 2.5 min. The data points are the average values over three replicates taken on three different gates. The blue dots are evaluated after incubation in the reference fluid (PBS), while the red ones are measured after incubation in PBS added with a single marker. The gray shaded area is the standard deviation over the three replicates. The black dashed lines in the rightmost panels are the relative current changes measured on the lateral gate serving as reference electrode. The limit-of-identification (LOI) level is also shown as a dashed-dotted black line (see text for details).

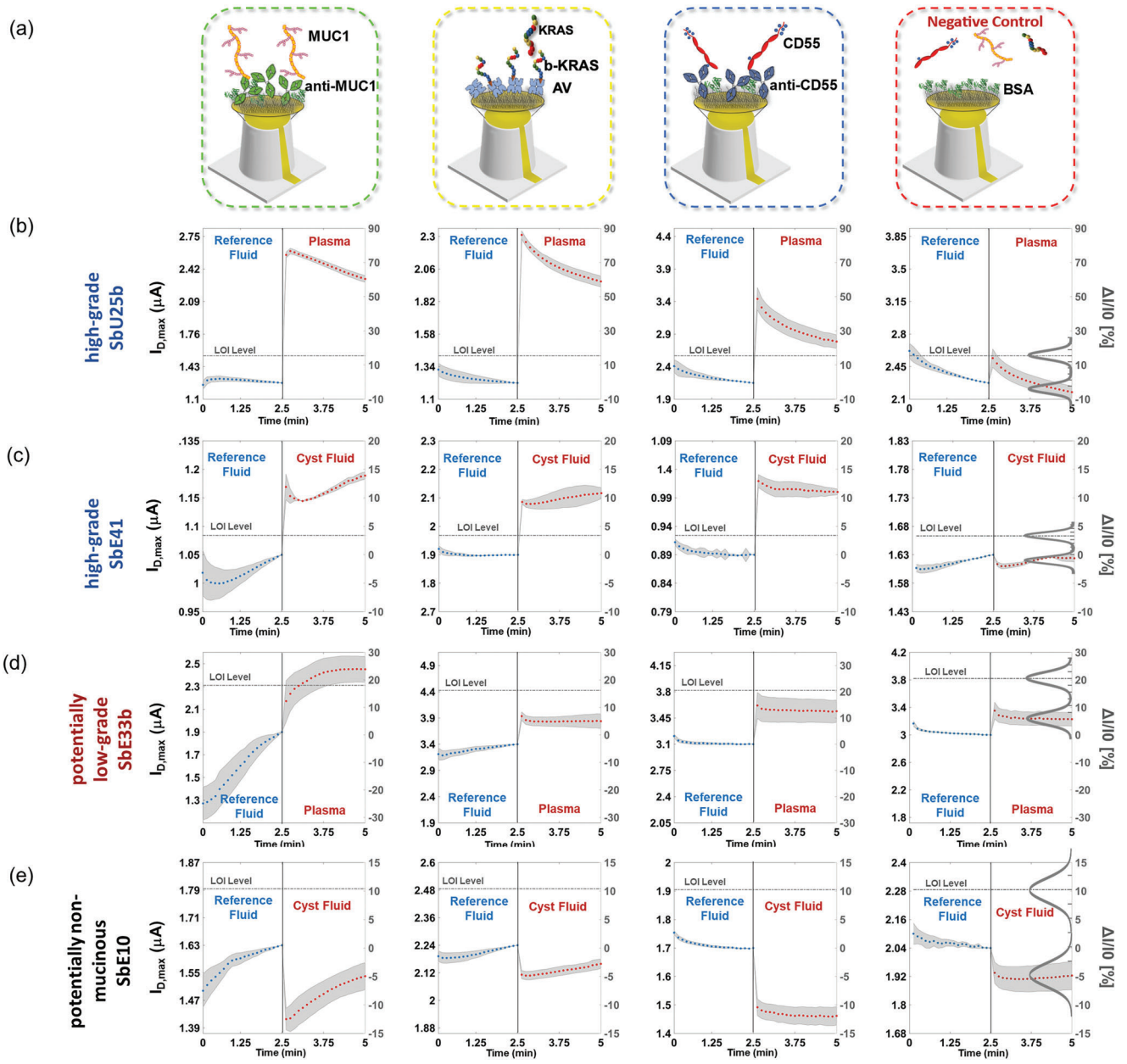

Figure 6. MUC1, KRAS^{mut}, and CD55 SiMBiT sensing measurements according to the protocol described in Figure 4, carried out in real patients' cysts fluid or blood plasma. In (a) the schematics of the gate pillars illustrating the chem-SAM, the capturing recognition elements (anti-MUC1, b-KRAS^{mut}, and anti-CD55), and their affinity ligands, are shown. The rightmost panel shows the data taken with BSA biofunctionalized gates serving in the negative control experiments. In the other panels, the assays of the MUC1, KRAS^{mut}, and CD55 are sequentially (left to right) featured. The dots are the data points relevant to the I_D values (left axis), and their relative changes, $\Delta I/I_0 = (I - I_0)/I_0$ (right axis, currents measured in water at $V_{GS} = -0.5$ V, $V_D = -0.4$ V) vs cycles (top *x*-axis) and time (bottom *x*-axis), during 20 cycles (2.5 min). b–e) The blue dots are the current data-points taken after incubation in the reference fluid (PBS) while the red dots are taken after incubation in the real fluid for cysts diagnosed as: b) high-grade mucinous in plasma, c) high-grade mucinous in cyst fluid, d) potentially low-grade mucinous (no evidence of high-grade mucinous) in plasma and, e) potentially nonmucinous (no evidence of mucinous) in plasma. The sensing data are the average over three replicates while the negative control experiments are averaged over seven replicates. The shaded area is one standard deviation. The dark-gray dashed-dotted lines are the limit-of identification (LOI) levels.

(see Figure S9b in the Supporting Information). In **Figure 7**a the *scores* on PC1 and PC2 are plotted showing clear graphical clustering of high-grade (blue triangles) while the potentially low-grade (red circles), and the potentially nonmucinous cysts (black squares) samples overlap to a large extent. The larger hollow symbols are the data points relevant to the sensing current traces taken from the samples featured in Figure 6. The mucinous high-grade cysts cluster at positive scores of PC1 while the potentially low-grade cysts and the potentially nonmucinous ones fall at negative PC1 values. In Figure 7b the loadings on PC1 and PC2 are

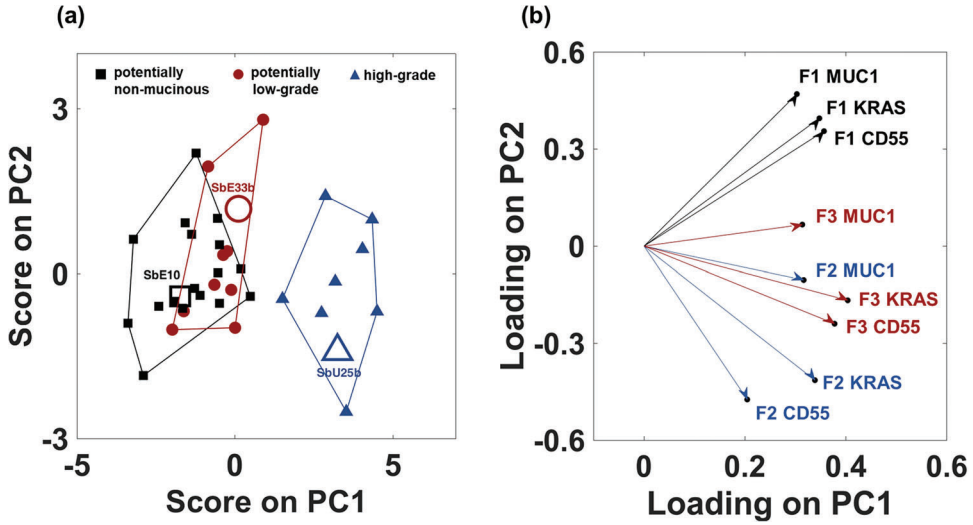

Figure 7. a) Score-plot featuring the score of each sample evaluated for the two principal components PC1 and PC2. The data shown as blue labels belong to the high-grade mucinous cysts, the red label to the potentially low-grade mucinous cyst (no evidence of high grade), and the black to the potentially nonmucinous samples (no evidence of mucinous). b) Loading scatter plot, showing the loadings of each original feature on PC1 and PC2; the F1, F2, and F3 features are indicated with black, blue and red arrows, respectively.

shown, providing the weights for the F1, F2, and F3 features. The following can be observed: i) the presence of either one of the features (for all three markers) is evidenced by positive PC1 loadings; ii) the presence of the two protein markers is partially decoupled by opposite PC2 loadings, namely: CD55 is characterized mostly by negative loadings while MUC1 by very positive one; iii) $KRAS^{mut}$ holds a weakly positive loading for PC2. While the high-grade samples cluster shows no overlap with the others, a confusion area is present for the potentially low-grade and the potentially nonmucinous cysts.

To reach a classification among the high-grade and the potentially low-grade and the potentially nonmucinous ones, a machine-learning approach is undertaken. To this aim a *k*-NN[68] classifier was adopted and instructed on the training set (37 patients), while its predictive performance was evaluated on the external test set (10 patients). To prevent overtraining, the latter was not used for algorithm training. As customary, the *k*-NN delimiting function was evaluated iteratively 10 times in cross-validation. Each time, 4 random samples were assigned to an evaluation set, while the other 33 samples were used to develop the *k*-NN delimiting function. This procedure led to the misclassification of only one sample (SbE19b marked in bold italics in the table in the "SiMBiT Machine-Learning-Based Discriminant Classifier part of the Experimental Section"). Specifically, in this training set a potentially low-grade cyst was erroneously classified as potentially nonmucinous, leading to one false negative over the whole set of 47 patients. In a preoperative assessment the SbE19b patient was diagnosed as potentially nonmucinous by histocytopathology analysis complemented by NGS. The corresponding blood sample was analyzed by SiMBiT. Eventually, the patient was surgically resected, and it was finally diagnosed as potentially low-grade.

To test the predictive power of the model, the computed *k*-NN model was used to classify the samples of the external test set (in a double-blinded way), returning the output shown in

Table 1. Output of the *k*-NN classifier on the external test set benchmarked toward diagnoses.

	Patient	Cyst class prediction	Diagnosis
External test set	SbG2	Potentially nonmucinous[a)]	Potentially nonmucinous[a)]
	SbG3	Potentially nonmucinous[a)]	Potentially nonmucinous[a)]
	SbE51	Potentially low-grade mucinous[b)]	Potentially low-grade mucinous[b)]
	SbE60	Potentially low-grade mucinous[b)]	Potentially low-grade mucinous[b)]
	SbE6	Potentially low-grade mucinous[b)]	Mucinous (no grading)
	SbE26	High-grade mucinous	Mucinous (no grading)
	SbE41	High-grade mucinous	Mucinous (no grading) [c)]
	SbG4	Potentially nonmucinous[a)]	Potentially nonmucinous[a)]
	SbG11	Potentially nonmucinous[a)]	Potentially nonmucinous[a)]
	SbG12	Potentially nonmucinous[a)]	Potentially nonmucinous[a)]

[a)] No evidence for mucinous; [b)] No evidence for high-grade; [c)] Presence of aneuploidy (abnormal DNA content) that might suggest this mucinous being high-grade.

Table 1, where the outputs of the classifier are benchmarked against the actual diagnosis. As it is apparent, the SiMBiT classifier has correctly predicted all the external test-set samples being in perfect agreement with the diagnosis. Moreover, the SiMBiT classifier is proven capable also to discriminate the grading of the SbE6, SbE26, and SbE41 samples, ascribed generically to mucinous neoplasms by the state-of-the-art diagnosis. For SbE6 and SbE26 the grading was not possible due to the absence of epithelial cells at cytology and of gene mutations known to correlate with high-grade features. For SbE41 the presence of aneuploid DNA content along with a reduced CDKN2A gene dosage (NGS of cell-free DNA) could possibly indicate a high-grade lesion.

This, strikingly, in agreement with the SiMBiT classification. Histologic confirmation, however, is still missing. The capability

Table 2. Overall diagnostic-sensitivity and diagnostic-specificity for SiMBiT based on all the 47 samples data set, benchmarked against state-of-the-art diagnosis.

Technology/approach	Body fluid	Markers assayed	Diagnostic	Mucinous [%]	High-grade mucinous [%]
Histo-cytopathology + NGS (state-of-the-art)	Cysts fluid	KRAS[a] GNAS[a] TP53[a]	Specificity	100	100
			Sensitivity	92	60
SiMBiT	Cyst fluid/blood plasma	MUC1[b] CD55[b] KRAS[a]	Specificity	**100**	**100**[c]
			Sensitivity	**96**	**100**[c]

[a] Nucleic acid mutations; [b] Protein; [c] These are evaluated only on the training set as there was lacking state-of-the-art diagnosis on samples: SbE6, SbE26, SbE41.

of the SiMBiT platform to better grading the samples analyzed is most likely related to its capability to detect the CD55 and the MUC1 at the single-molecule level.

The results for the diagnostic-sensitivity (relative incidence of false-negatives) and the diagnostic-specificity (relative incidence of false-positives) percentages are provided on the whole cohort of patients in **Table 2**. Here the sorting into mucinous and high-grade is shown against the standard diagnosis. The figures of merit of the SiMBiT classifier, operating only on the preoperative samples, are based on both the training set and test set. As it is evident the SiMBiT platform, operating also on plasma samples, outperforms state-of-the-art diagnosis being more accurate, particularly in terms of diagnostic-sensitivity. However, it is worth underlying that these results are based on a preclinical set of 47 patients and that a more robust reliability assessment based on more patients, is ongoing.

Finally, the SiMBiT assay time-to-results per 5–6 patients is only 90 min with an overall estimated cost (including personnel) per 5–6 patients of less than 100 € (see also Section S6 in the Supporting Information). Standard diagnosis requires from 3 to 10 days and costs are of about several hundred euros.

3. Conclusion

A portable bioelectronic platform ($18 \times 11.5 \times 4.5$ cm^3) for a multiplexing single-molecule sensing array is here proposed. It is composed of a disposable cartridge that incorporates an array of 96 electrolyte-gated organic transistors with lateral reference gates, manufactured on a plastic foil, glued to a bottomless standard ELISA plate, whose wells hold the electrolyte. Organic thin film transistor multiplexing electronics enables reading all sensors within the same form factor of the standard ELISA plate. The cartridge is supplemented by a 3D-printed cover plate of sensing gates that protrude into each well. These gates are biofunctionalized with the recognition element (capturing antibodies or probes) to simultaneously assay proteins and nucleic acid biomarkers in a real biofluid. A reusable reader based on a PCB and a custom Si-IC chip provides miniaturized and accurate digitalization of the data, together with all electronic support functions. The prototype can be operated through software that is installed on a USB-connected smart device.

The 8×12 multiplexing array prototype developed at TRL5 is uniquely capable of reliably performing simultaneous single-proteins and single-copy-DNA assay. The oncoproteins (MUC1, CD55) and mutated nucleic acid (KRAS^{mut}) are detected in the cyst fluid or the blood plasma of 47 patients to identify mucinous cysts and sort those with high-grade features, recognized as precursors for pancreatic cancer. The multiplexing detection of the three target biomarkers is performed in triplicates, along with 7 negative-control experiments for 5 to 6 different patients tested with one plate. A machine-learning-based classifier is fed with the data of 37 patients' samples and its prediction capabilities are challenged using an external test-set of 10 samples analyzed in a double-blinded way. Remarkably, the analysis of all three SiMBiT markers in the 47 patients resulted in at least 96% diagnostic-sensitivity and 100% diagnostic-specificity for the detection of mucinous neoplasms as well as for the sorting of those with high-grade features in cyst fluids as well as in blood plasma. In addition, the SiMBiT technology is more cost-effective and faster than state-of-the-art diagnostic procedures, being also the only assay allowing for simultaneous testing of protein and genomic markers both at the single-molecule level.

This preclinical study, though based only on a cohort of 47 patients, offers a compelling proof-of-principle that opens a completely new highway toward liquid biopsy in blood plasma for pancreatic cancer screening and holds the potential of saving millions of persons in the future.

4. Experimental Section

Materials: The materials used in the experiment included Bovine serum albumin (BSA), high-purity ethanol, avidin from egg white, poly(3-hexylthiophene) (P3HT), and phosphate buffer saline (PBS tablets), all purchased from Sigma-Aldrich without the need for further purification. The device components, such as the lateral gate and interdigitated source-drain gold electrodes, were patterned with a lift-off photolithography process on a poly(ethylene 2,6-naphthalate) (PEN) substrate, 125 micrometers thick purchased from Du Pont. The monoclonal antibodies for Mucin 1 (anti-MUC1) and the recombinant protein of human Mucin 1 were provided by OriGene. CD-55 monoclonal antibodies (anti-MUC1, clone 1D7 and clone 1G3) and the recombinant protein of human complement decay-accelerating factor (CD-55, M_W = 67 800 Da, product number: H00001604-P01) were provided by Abnova. Invitrogen–Thermo Fisher Scientific was the source of mutated nucleic acids KRAS (KRAS^{G12D}) which were utilized without any modifications. The biorecognition element, also known as the probe, was Biotinylated-KRAS^{G12D} fwd with a molecular weight of 7.914 Da and a sequence of 5′-TGCCTACGCCATCAGCTCCAACTAC. The target oligonucleotides, referred to as KRAS^{G12D}, had a molecular weight of 7,835 Da and a sequence of GTAGTTGGAGCTGATGGCGTAGGCA. The MerckMillipore company (now MilliporeSigma) provided the 3-mercaptopropionic acid (3-MPA), 11-mercaptoundecanoic acid (11-MUA), 1-ethyl-3-(3-dimethylaminopropyl) carbodiimide (EDC), and *N*-hydroxysulfosuccinimide sodium salt (Sulfo-NHS) used in the study. Quanterix provided Tween 20, Sulfosuccinimidyl 4-[*N*-maleimidomethy]

cyclohexane-1-carboxylate (Sulfo-SMCC), 1 M Tris HCl pH 7.4, NHS-PEG4-Biotin, Streptavidin Horseradish Peroxidase (SA-HRP), Horseradish Peroxidase Substrate (SuperSignal Luminol), and sample diluent (Phosphate buffer with BSA and sodium azide as preservative). Universal ELISA plates with an immobilized protein anchor were purchased from Quanterix and stored at 2–8 °C.

SiMBiT 8 × 12 Electrolyte-Gated Organic Field-Effect Transistors (EGOFETs) Array Fabrication: To fabricate the EGOFET array, a flexible 125 µm thick PEN foil was used. The gold lateral gate, along with the source and drain electrodes, was designed on the PEN substrate through a lift-off photolithography technique that used a reverse flood exposure process. A coplanar lateral gate configuration was chosen to better fit the bottom of an ELISA well, while PEN was chosen as it is robust, cheap, enables an effortless bonding with the addressing electronics, and can be easily glued to the ELISA plate, preventing water leaking. To complete this process, only one layer of photoresist (AZ5214E – MicroChem) was needed. Initially, the photoresist was spin-coated onto the substrate for 60 seconds at 4000 rpm, then baked at 110 °C for 90 s to eliminate the solvent, and then negatively exposed using a mask aligner (Karl Süss MA6/BA8) with a custom-made negative photolithographic mask (created by CompuGraphics). The exposed parts of the resist were then crosslinked by baking at 120 °C for 90 s. The desired pattern was obtained after the complete sample was exposed to floods and subsequently developed in AZ 726 MIF developer. A chromium adhesion layer (2 nm) was deposited on the PEN substrate before the thermal evaporation of gold (30 nm). To complete the lift-off step, the sample was immersed in TechniStrip Microdeposit D2 stripper overnight. Afterward, the samples were cleaned in both acetone and IPA using an ultrasonic bath, dried with nitrogen, and further cleaned with oxygen plasma for 2 min. An interdigitated electrode structure was chosen to increase the width/length ratio and improve the transistors source–drain current. The dimensions of the structure were: channel width of 10^4 µm, channel length of 5 µm, and a circular lateral gate diameter of 2.5 mm. A biocompatible insulator film (SU8 – TF6001 MicroChem) was inkjet printed by a Fujifilm Dimatix DMP-2831 on top of the gold traces exposed to the electrolyte, except for the channel and the lateral gate areas, using a cartridge with 10 pL nozzles. Finally, the P3HT organic semiconductor was deposited only on the gold source and drain contacts through ink-jet printing. The plate temperature was set to 35 °C while printing the organic semiconductor with a drop spacing of 45 µm and firing voltage of 40 V. Additionally, the jetting frequency used was 1 kHz during the printing process. The inkjet printing of the organic semiconductors was optimized to improve the electrical performance of the SiMBiT devices, namely the on/off ratio, the maximum I_D current, and the I_D/I_G ratio. To this aim, P3HT in a blend of ortho-dichlorobenzene (ODCB) and chlorobenzene (CB)—in a ratio of 25/75 ODCB/CB—with a concentration of 2.6 mg mL^{-1} resulted to be the best formulation. As a final step, a standard black bottomless ELISA plate with 96 wells (Greiner Bio-One) was glued over the plastic foil with a medical-grade double-sided adhesive foil. The dark colour prevents the P3HT device from being exposed to light. Each well of the plate was filled with 320 µL of water (HPLC-grade, Honeywell Riedel-de Haën) serving as the gating medium.

Fabrication of the 3D-Printed Sensing Gates Cover Plate: The 3D sensing gate plate consists of 96 hollow pillars that protrude 6.5 mm. A 0.3 mm thick cavity prevents any metal interconnections to be in contact with the ELISA plate surface. The top base radius of each pillar is 2.8 mm, while the bottom base radius is 3.25 mm with a side wall slope of 3.9°. The plate was patterned and optimized to fit into a commercial ELISA plate during its biofunctionalization and sensing measurements. Additive printing techniques were used for the fabrication of the 3D structures, specifically a 3D printing stereolithography approach. This approach was chosen for its fast and flexible design, low costs, no material waste, high accuracy, and wide range of materials suitable for various experimental conditions and applications. The Form 2 printer was utilized for this purpose with a layer thickness of 100 µm, raft type: full raft, density: 1.20, touchpoint size: 0.45 mm, height above rafts: 10.00, raft thickness: 2.00 mm, tilt angle $\alpha_x = \alpha_y = 45°$. The Clear Resin FLGPCL04 is a commonly used material for high-quality rapid prototyping due to its excellent solvent compatibility, good temperature properties, and ability to produce high-resolution results. After the printing process, the samples are post-cured through a combination of annealing and UV exposure. This involves placing the samples in a UV oven at 65 °C for 20 min to ensure uniform heating before exposing them to UV light for 30 min. The curing rate of the resin is dependent on its temperature, making it essential to maintain a uniform temperature throughout the process to minimize residual stress. The roughness of the 3D sensing gate plates is reduced before e-beam evaporation by depositing a 2 µm layer of Parylene-C.[29] The coating thickness of Parylene-C remains constant regardless of the shape of the substrate, and it does not have any pinhole. It is also biocompatible and has excellent chemical stability with a wide range of solvents, including those used for gate biofunctionalization such as ethanol, PBS, and water. The deposition of Parylene-C was done via chemical vapor deposition using a Labcoter PDS 2010 from SCS. The process involved placing 4 grams of solid dimer inside the vaporization chamber, which sublimates at 175 °C and converts to the monomer phase at 690 °C under a pressure of 0.5 Torr. At room temperature and a pressure of 0.01 Torr, the monomers undergo polymerization in the polymerization chamber by forming covalent bonds with each other until the polymeric chains become long enough to attach to the substrate due to gravity. Subsequently, a planarization step is performed, followed by the direct e-beam evaporation of gold onto the 3D gate plate structure with Parylene-C, with a thickness of ≈150 nm. The 3D sensing gate plates are then cleaned with IPA and subjected to a plasma oxygen treatment for 120 s using the Plasma Asher model Femto from Diener Electronic, with an O_2 pressure of 0.4 mbar and power of 100 W.

Sensing Gates Bio-Functionalization Protocol: The gate biofunctionalization is carried out by immersing the 3D sensing gate plate into a standard 96-well plate, filled with the needed biofunctionalization solutions. The first step in the protocol involves immobilizing a chemical SAM (chem-SAM) on a gold surface using a solution containing 10×10^{-3} M of 3-MPA and 11-MUA (10:1 molar ratio) in ethanol. The gold-coated pillars of the 3D sensing gate plate are dipped in this solution and left in the dark under N_2 atmosphere for 18 h at room temperature (25 °C). This creates a monolayer known as the chem-SAM, which exposes carboxylic groups of the alkylthiols through covalent gold-sulfur interaction. These groups are activated by reacting with a 200×10^{-3} M solution of 1-ethyl-3-(3-dimethylaminopropyl) carbodiimide (EDC) in the presence of a 50×10^{-3} M sulfo-*N*-hydroxysuccinimide (sulfo-NHS) aqueous solution for 20 min at 25 °C. Following this, the biofunctionalization protocol proceeds with the immobilization of antibodies capturing layers, such as either i) anti-MUC1 and anti-CD55, or ii) a genomic biorecognition element (probe), b-KRAS^{mut}. i) To attach anti-MUC1 and anti-CD55 antibodies to the activated –COOH sites, the gate surface was submerged in PBS solutions of each antibody for 2.5 h at 25 °C. These solutions contained 133×10^{-9} M (20 µg mL^{-1}) of the respective antibody in PBS with a pH of 7.4 and an ionic strength of 163×10^{-3} M. Unreacted sulfo-NHS ester groups were then saturated with ethanolamine (1 M in PBS) for 45 min at 25 °C, and finally, the bio-functionalized gate was submerged in a 1.5×10^{-3} M (0.1 mg mL^{-1}) BSA solution in PBS for 1 h at 25 °C to reduce nonspecific binding. ii) When dealing with probes, the gate surface with activated carboxylic groups was submerged in an AV phosphate buffer saline solution for two and a half hours at room temperature. The solution contained 833×10^{-9} M of AV in PBS at pH 7.4. Following this, the AV-modified SAM underwent further treatment with ethanolamine 1 M in PBS for 45 min at room temperature. Afterwards, the gate surface was immersed in a biotinylated KRAS^{mut} 0.5×10^{-6} M PBS solution at pH 7.4 for 1 h at room temperature. After each step of biofunctionalization, the gate was washed with the corresponding solvent to remove any unbonded residues. In the negative control experiment, the pillars of the 3D sensing gate plate were biofunctionalized with only BSA according to the same protocol used for the antibodies. The entire biofunctionalization process was carried out by filling a standard 96-well ELISA plate with a volume of 100 µL of solution for each reagent. The 3D sensing gate plates were designed to test for three biomarkers from six patients at the same time. This means that each patient's biomarkers can be tested in triplicate on a single 3D sensing gate plate, along with seven negative control experiments.

Biomarkers Standard Solutions in PBS: To simulate blood plasma conditions, standard solutions of MUC1, KRAS^{mut}, and CD55 in PBS with an ionic strength of 163×10^{-3} M and a pH of 7.4 were prepared by diluting stock solutions. The dilution process followed the equation $c_2 = c_1V_1/V_2 = kc_1$, where c_1 and c_2 represent the initial and diluted ligand concentrations, respectively, and V_1 and V_2 are the corresponding solution volumes. The dilution factor, represented by $k = V_1/V_2$, was used to calculate the concentrations. The stock solution was used for subsequent dilutions in the tenfold serial dilution series starting from the concentrated analytes' mother solution. The absolute uncertainty on each concentration of the standard solutions was calculated as the propagation error of the dilution factor, while the uncertainty of the volume, given by the supplier company of the pipettes used, is 1%. This value of the uncertainty of the volume considers both random and systematic errors in pipetting. The nominal number of target molecules at a concentration is determined using the equation cVN_A, where c is the analyte concentration, V is the volume of the standard PBS solution used (150 µL), and N_A is the Avogadro number. For very low concentrations, Poisson's distribution can be used to estimate the error associated with the sampling procedure. The total uncertainty of the ligand concentration is obtained by adding the squares of the dilution (σ_D) and Poisson's (σ_P) errors and taking the square root of the sum. This means that the 150 µL of PBS standard solution, in which the sensing gate was incubated, at a concentration of 10 zM 1 ± 1 molecules are present. Therefore, according to Poisson's distribution, there is a 64% probability that in a 10 zM solution there is at least one molecule.

Collection of Body Fluids: Pancreatic cyst fluids (1–5 mL) were withdrawn during routine diagnostic and/or therapeutic interventions, such as endoscopic ultrasound fine-needle aspiration. Venous blood was collected in Cell-Free DNA BCTs tubes (Streck, Nebraska, US) following the manufacturer's instructions. Samples were sent immediately to the Institute of Pathology for further processing. If immediate shipping was not possible, samples were stored at 4 °C. Prior to cfDNA isolation, plasma was separated from 10 mL whole blood by centrifugation at 600*g* for 20 min. Plasma samples were then centrifuged at 1600*g* for 10 min at room temperature to remove any remaining cells. cfDNA was extracted using QiAamp circulating nucleic acid kit (Qiagen, Hilden, Germany) and quantified by a custom-made qPCR assay (Primer for: 5′-AAACGCCAATCCTGAGTGTC-3′; Primer rev: 5'CATAGCTCCTCCGATTCCAT-3′).

Tissue samples consisted of specimens obtained by fine-needle biopsy or resection specimens acquired through surgery. Samples were fixed in 4% buffered formaldehyde and embedded in paraffin. Hematoxylin & Eosin stains were prepared from 2-µm sections of formalin-fixed paraffin-embedded (FFPE) tissues. These stains were evaluated to determine a sample area suitable for DNA isolation. DNA from tissue was extracted using GeneRead DNA FFPE Kit (Qiagen, Hilden, Germany) following the manufacturer's instructions. The human plasma samples were centrifugated at 10 000*g* for 5 min to remove insoluble material and then diluted 1:8 (v/v) with PBS reference fluid before testing. The human cyst fluids were diluted as received 1:8 (v/v) in PBS reference fluid. For both plasma and cyst fluids, an aliquot of each diluted sample was heated up in a water hot bath at 90 °C for 3 min prior to the analysis with b-KRAS^{mut} modified gates.

All individuals provided their informed consent for participation before being included in the study (Patients' information and informed consent—University Hospital of Düsseldorf). The study was conducted in compliance with the Declaration of Helsinki and the EU General Data Protection Regulation (EU-GDPR). Additionally, the protocol for analyzing body fluids and tissues received approval from the Ethics Committee of the University Hospital of Düsseldorf (Project H2020 SiMBiT GA 824946).

SiMBiT Sensing Measurements: The 8 × 12 SiMBiT array was kept in contact with HPLC-grade water (conductivity 0.056 µS cm^{-1}) dispensed into the 96 wells for about 24 h. Afterward, the source–drain current I_D was stabilized by cycling the measurement of the transfer characteristics using the reference lateral gate, namely I_D vs V_{GS} ranging from 0 to −0.5 V at fixed V_D of −0.4 V, every half an hour, until the current drift was reduced to 1% h^{-1}.[65] The 3D sensing gate plate, properly biofunctionalized for the simultaneous proteins or genomic assay, was stored in a standard ELISA plate filled with PBS and washed thoroughly with HPLC water prior to the assay. As a first step, the 3D sensing gate plate was incubated in a standard ELISA plate filled with 150 µL of PBS, used as a reference fluid, for 10 min. The 3D sensing gate plate was then washed thoroughly with HPLC water using a custom wash tank, and a stable baseline (I_0) was acquired, measuring 20 subsequent transfer characteristics (2.5 min). The reiterated measurement of a set of 20 transfer curves, is addressed as "cycling" which is always carried out in HPLC water. The same 3D sensing gate plate was further incubated in the samples, diluted 1:8 (v/v) in PBS for 10 min, and then washed thoroughly with HPLC water. A second set of 20 transfer characteristics was acquired in 2.5 min, thus providing the signal *I*. During both incubation steps in the reference fluid as well as in the sample solutions, the stability of the SiMBiT array was assessed registering the I_D current level with the coplanar reference lateral gates. Even in this case sets comprising 20 transfer characteristics were registered in the same voltage window of the 3D sensing gate plate. All data acquired during the experiments were plotted and analyzed using MatLab software.[69] A video illustrating the whole procedure is provided in Movie S1 (Supporting Information).

Assessment of the Limit-of-Identification (LOI): The SiMBiT platform provides a yes/no-type of response with the threshold at the limit-of-identification (LOI). The LOI level defines the smallest amount of an analyte (e.g., the targeted marker) that can be distinguished from the noise level (random error) at a level of confidence better than 99%, namely with an incidence of false-positives and false negative lower than 1%.[70] This is assured by taking the LOI level at the noise-average-level (μ_n) + 6 times the noise-standard-deviation (6σ).[14] The Gaussian distribution of the noise's standard deviation (assumed to be the same of the sample to be assessed), was evaluated through a set of negative control experiments. Namely: i) for the experiments carried out in PBS, the LOI level was estimated from 7 negative control experiments encompassing BSA functionalized gates exposed to a PBS solution containing MUC1, KRAS^{mut}, and CD55 (10×10^{-9} M); ii) for the patients' samples (both cyst fluid and blood plasma diluted 1:8 (v/v) in the reference fluid) the LOI level was estimated for each patient from 7 negative control experiments, registered with BSA biomodified gates exposed to 150 µL patient's sampled solution.

SiMBiT Machine-Learning-Based Discriminant Classifier: A machine-learning approach was undertaken to analyze the whole data set collected on 47 patients' samples (12 plasma samples and 35 cysts fluids). The data set was divided into a training set consisting of 37 samples, used to instruct the model, and a test-set of 10 samples analyzed in double-blinded, used to verify the predictive capability of the model. For each patient fluid, the analysis of MUC1, KRAS^{mut} and CD55 was accomplished simultaneously, along with 7 negative control experiments. The data from the negative control experiments served to define LOI level (vide supra). The summary of the measurements is given in Table 1, along with the final diagnosis. The biofluid in which the SiMBiT analysis was performed is given as well. For each biomarker, the three following features were estimated: i) $F1 = (I_{15-20} - I_{0\_15-20})/I_{0\_15-20}$ (average over three replicates), where $I_{15-20} = \frac{1}{5}\sum_{i=15}^{20} I \cdot (V_{GS} = -0.5\ V;\ V_D = -0.4\ V)$ is the sensing current averaged over the last 5 cycles (cycles 15–20) after exposure to a patient sample, while the $I_{0\_15-20} = \frac{1}{5}\sum_{i=15}^{20} I_0(V_{GS} = -0.5\ V; V_D = -0.4\ V)$ is the baseline current averaged over the last 5 cycles after incubation in the PBS reference fluid. Those values are calculated using the NumPy package with numpy.mean() in Python. ii) $F2 = (I_{20} - I_1)/(I_{0,20} - I_{0,1})$, where I_1, I_{20}, $I_{0,1}$, $I_{0,20}$ are the I and I_0 current values (at $V_{GS} = -0.5$ V and $V_{GS} = -0.4$ V) measured at cycles 1 and 20. This feature correlates to the normalized dynamic drift of a given gate. iii) *F3* is the yes/no (0, 1) binary variable defined as 0 when the $\Delta I/I_0 \leq$ LOI level or 1 when $\Delta I/I_0 >$ LOI. A graphical representation of the features can be found in Figure S8a (Supporting Information). The machine-learning algorithm herein developed has the main goal to perform discriminant classification of the samples belonging to the high-grade, low-grade mucinous cyst or nonmucinous classes. To this aim a *k*-NN classifier[68] was coached on the training set, as defined in **Table 3**, comprising 37 samples, while its predictive performance has been evaluated on the external test set of 10 samples, to prevent the overtraining of the model. The core of the *k*-NN depends on a "guilt by association" principle where classification is performed by measuring the

Table 3. List of the patients' samples assayed in the pre-clinical trial used as "training" and "external-test set", along with the assayed fluids, and the average AI features values extracted for MUC1, KRAS^{mut}, and CD55 over three replicates. The diagnosis formulated by the pathologists is provided only for the training set.

				MUC1			KRAS			CD55		
	Patient	Diagnosis	Fluid	F1	F2	F3	F1	F2	F3	F1	F2	F3
Training set	SbU18b	**High-grade mucinous cyst (# 9)**	Plasma	0.22	1.65	1	0.14	2.67	1	0.14	0.48	1
	SbU25b		Plasma	0.60	1.50	1	0.61	0.98	1	0.27	0.57	1
	SbE38b		Plasma	0.13	0.68	1	0.17	0.81	1	0.54	0.25	1
	SbE5		Cyst fluid	0.25	0.62	1	0.16	0.86	1	0.18	0.82	1
	SbG1		Cyst fluid	0.14	4.55	1	0.20	2.00	1	0.57	0.35	1
	SbE15		Cyst fluid	0.69	0.68	1	0.27	1.11	0	0.39	0.04	1
	SbE18		Cyst fluid	0.14	1.74	1	0.03	5.00	1	0.13	0.50	1
	SbE32		Cyst fluid	0.19	2.82	1	0.00	0.00	0	0.09	0.17	1
	SbE43		Cyst fluid	0.86	1.80	1	0.20	1.00	1	0.27	1.11	1
	SbE30b	**Low-grade mucinous cyst (# 10)**	Plasma	0.07	0.81	1	−0.02	0.22	0	−0.03	2.25	0
	SbE33b		Plasma	0.37	0.51	1	0.09	−1.00	0	0.11	−0.70	0
	SbE31		Plasma	0.18	1.09	1	0.01	−0.78	0	0.04	−6.67	0
	SbE53		Plasma	0.08	0.63	1	−0.26	−1.39	0	−0.29	−0.64	0
	SbE49b		Plasma	0.19	1.69	1	−0.02	0.07	0	−0.12	−0.29	0
	SbE1		Cyst fluid	0.09	0.33	1	−0.07	0.00	0	−0.07	−0.96	0
	SbE3		Cyst fluid	0.48	1.40	1	0.34	−2.00	0	0.32	−1.91	0
	SbU47		Cyst fluid	0.19	0.52	1	0.04	−0.59	0	0.01	−0.54	0
	SbE37		Cyst fluid	0.07	1.40	1	0.05	−1.00	0	−0.02	−1.05	0
	SbE19b		***Plasma***	***0.16***	***0.95***	***0***	***−0.30***	***−0.69***	***0***	***−0.30***	***−0.57***	***0***
	SbE50b	**Non-mucinous (# 18)**	Plasma	−0.37	−0.41	0	−0.32	−0.67	0	−0.26	−0.63	0
	SbG21		Plasma	−0.31	−1.26	0	−0.31	−0.65	0	−0.28	−3.77	0
	SbE2		Cyst fluid	0.14	1.31	0	0.04	−0.07	0	0.05	−0.46	0
	SbE4		Cyst fluid	−0.11	−0.43	0	−0.09	−0.31	0	−0.02	−0.48	0
	SbE7		Cyst fluid	0.65	−0.38	0	0.00	0.00	0	−0.02	−1.00	0
	SbE8		Cyst fluid	−0.20	−0.80	0	−0.16	−0.67	0	−0.12	−2.00	0
	SbE9		Cyst fluid	−0.14	−2.38	0	−0.11	−3.24	0	−0.09	−2.23	0
	SbE10		Cyst fluid	−0.04	−0.92	0	−0.04	−0.60	0	−0.07	−0.25	0
	SbE16		Cyst fluid	0.24	0.58	0	−0.13	−0.50	0	0.34	−7.00	0
	SbE17		Cyst fluid	0.12	−1.15	0	0.03	−1.25	0	0.07	−2.00	0
	SbE22		Cyst fluid	0.18	0.91	0	−0.17	−0.50	0	0.00	0.00	0
	SbE23		Cyst fluid	−0.02	−2.26	0	0.23	−1.11	0	0.09	−0.26	0
	SbE24		Cyst fluid	−0.02	0.00	0	−0.15	−1.14	0	−0.10	−0.50	0
	SbE25		Cyst fluid	0.12	1.11	0	0.01	0.14	0	0.03	1.00	0
	SbE28		Cyst fluid	0.13	2.90	0	0.11	1.00	0	0.14	0.60	0
	SbE29		Cyst fluid	0.00	0.00	0	−0.01	−0.68	0	0.00	0.00	0
	SbE34		Cyst fluid	0.15	0.52	0	0.19	0.67	0	0.21	1.00	0
	SbE45		Cyst fluid	0.24	0.39	0	0.08	0.73	0	0.07	−1.94	0
External test set	SbG2		Cyst fluid	−0.13	−9.00	0	−0.11	−3.50	0	−0.12	−1.84	0
	SbE60		Plasma	0.33	0.96	1	0.13	0.33	0	0.18	−1.83	0
	SbG3		Cyst fluid	−0.11	−0.77	0	−0.13	−0.42	0	−0.20	−1.80	0
	SbE51		Cyst fluid	0.34	1.64	1	0.22	−0.70	0	0.27	−2.26	0
	SbE6		Cyst fluid	0.45	4.33	1	−0.28	−0.20	0	−0.34	−4.00	0
	SbE26		Cyst fluid	0.28	0.81	1	0.25	1.00	1	0.06	0.67	1
	SbE41		Cyst fluid	0.17	0.59	1	0.01	0.25	0	0.11	0.23	1
	SbG4		Cyst fluid	−0.16	−3.50	0	−0.40	−1.83	0	0.08	−5.00	0
	SbG11		Cyst fluid	0.04	0.28	0	0.06	0.70	0	0.17	−3.33	0
	SbG12		Cyst fluid	0.06	0.46	0	−0.04	−4.00	0	0.02	−1.50	0

similarity between a query and a set of training patterns, computed as distances. Specifically, it is a nonlinear discriminant classification technique, based on the evaluation of the distances of a query object from all the objects in the training set. The query object is thus classified in the category of the k closest object(s), where the k value defines how many neighbors will be checked to determine the classification of the specific query objects. The *k*-NN classification of the SiMBiT data set was developed using a *k* value equal to 3, to avoid ties in classification, and Canberra distance metrics were defined according to Equation (1):

$$d_{\text{Canberra}} = \sum_{i=1}^{n} \frac{|x_i - y_i|}{|x_i| + |y_i|} \tag{1}$$

estimating the closeness between 2 vectors **x** and **y**, with $\mathbf{x} = (x_1, x_2, ..., x_n)$ and $\mathbf{y} = (y_1, y_2, ..., y_n)$. A cross-validation with 10 cancellation groups was undertaken to optimize the model *k*-NN class delimiter. The *k*-NN algorithm was developed using the open-source software of CAT (Chemometric Agile Tool).[71]

The diagnostic-sensitivity and diagnostic-selectivity were evaluated as follows

$$\text{Sensitivity} = \frac{\text{TP}}{\text{TP} + \text{FN}} \cdot 100\% = 100\% \tag{2}$$

$$\text{Specificity} = \frac{\text{TN}}{\text{TN} + \text{FP}} \cdot 100\% = 100\% \tag{3}$$

where TP and TN are the numbers of true positive and true negative, while FN and FP are the numbers of false negative and false positive respectively.

Supporting Information

Supporting Information is available from the Wiley Online Library or from the author.

Acknowledgements

H2020 – Electronic Smart Systems – SiMBiT: Single-molecule bioelectronic smart system array for clinical testing (Grant agreement ID: 824946), NoOne-A binary sensor with a single-molecule digit to discriminate biofluids enclosing zero or at least one biomarker, ERC Stg2021, GA: 101040383, Svenska Tekniska Vetenskapsakademien i Finland and CSGI are acknowledged for partial financial support.

Conflict of Interest

The authors declare no conflict of interest.

Author Contributions

E.G., F.M., and L.S. contributed equally to this work. L.T. coordinated the SiMBiT project and the writing of the manuscript, supervised along with EM the sensing measurements performed by L.S., C.S., and M.C.; E.M. coordinated the machine-learning performed by M.C. and co-supervised with R.O. the physical device characterization performed by K.B.; I.E. coordinated the work on the histopathology and N.G.S. analyses and supervised L.H.; E.C. designed and coordinated the work on the integrated reader supervising the work of E.G., while P.L., M.T.M., and C.B. worked on its industrial scaling and the development of the app; F.T. conceived the 3D-gates structure with L.T. and G.S. and coordinated the work of V.M.D. and G.F. on the gate array design and fabrication while the metallization was performed by C.D.F.. M.C., F.M., and F.A.V. conceived the work related to the on-foil bioelectronic system, while M.W. and W.R. worked on its industrial scaling; M.C. and F.A.V. cosupervised the on-foil bioelectronic system fabrication performed by FM. E.M., E.G., L.S., F.A.V., E.C., F.T., contributed to the writing of the paper, which was read, revised and approved by all the authors.

Data Availability Statement

The data that support the findings of this study are available on request from the corresponding author. The data are not publicly available due to privacy or ethical restrictions.

Keywords

bioelectronics, biomarkers, early detection, pancreatic cancer precursors, printed-electronics, single-molecule-with-a-large-transistor, single molecules

Received: May 3, 2023
Revised: June 29, 2023
Published online:

[1] R. Liu, X. Wang, K. Aihara, C. Luonan, *Med. Res. Rev.* **2014**, *34*, 455.
[2] Y. Deng, Z. Sun, L. Wang, M. Wang, J. Yang, G. Li, *Front. Med.* **2022**, *16*, 157.
[3] J. D. Cohen, A. A. Javed, C. Thoburn, F. Wong, J. Tie, P. Gibbs, C. M. Schmidt, M. T. Yip-Schneider, P. J. Allen, M. Schattner, R. E. Brand, A. D. Singhi, G. M. Petersen, S. M. Hong, S. C. Kim, M. Falconi, C. Doglioni, M. J. Weiss, N. Ahuja, J. He, M. A. Makary, A. Maitra, S. M. Hanash, M. Dal Molin, Y. Wang, L. Li, J. Ptak, L. Dobbyn, J. Schaefer, N. Silliman, et al., *Proc. Natl. Acad. Sci. USA* **2017**, *114*, 10202.
[4] J. Tabernero, H. J. Lenz, S. Siena, A. Sobrero, A. Falcone, M. Ychou, Y. Humblet, O. Bouché, L. Mineur, C. Barone, A. Adenis, T. Yoshino, R. M. Goldberg, D. J. Sargent, A. Wagner, D. Laurent, M. Teufel, M. Jeffers, A. Grothey, E. Van Cutsem, *Lancet Oncol.* **2015**, *16*, 937.
[5] K. J. Land, D. I. Boeras, X. S. Chen, A. R. Ramsay, R. W. Peeling, *Nat. Microbiol.* **2019**, *4*, 46.
[6] C. Schulte, T. Barwari, A. Joshi, T. Zeller, M. Mayr, *Trends Mol. Med.* **2020**, *26*, 583.
[7] A. Shrivastava, T. Haase, T. Zeller, C. Schulte, *Front. Cardiovasc. Med.* **2020**, *7*, 601364.
[8] M. Ye, J. Wang, S. Pan, L. Zheng, Z. W. Wang, X. Zhu, *Mol. Ther. Oncolytics* **2022**, *24*, 101.
[9] G. Disanto, C. Barro, P. Benkert, Y. Naegelin, S. Schädelin, A. Giardiello, C. Zecca, K. Blennow, H. Zetterberg, D. Leppert, L. Kappos, C. Gobbi, J. Kuhle, *Ann. Neurol.* **2017**, *81*, 857.
[10] N. K. Singh, P. Ray, A. F. Carlin, C. Magallanes, S. C. Morgan, L. C. Laurent, E. S. Aronoff-Spencer, D. A. Hall, *Biosens. Bioelectron.* **2021**, *180*, 113111.
[11] E. Engvall, *Mol. Immunol.* **1971**, *8*, 871.
[12] S. Zhang, A. Garcia-D'Angeli, J. P. Brennan, Q. Huo, *Analyst* **2013**, *139*, 439.
[13] E. Macchia, K. Manoli, C. Di Franco, G. Scamarcio, L. Torsi, *Anal. Bioanal. Chem.* **2020**, *412*, 5005.
[14] M. Thompson, S. L. R. Ellison, R. Wood, *Pure Appl. Chem.* **2002**, *74*, 835.
[15] J. Wilhelm, A. Pingoud, *ChemBioChem* **2003**, *4*, 1120.
[16] J. M. Rothberg, W. Hinz, T. M. Rearick, J. Schultz, W. Mileski, M. Davey, J. H. Leamon, K. Johnson, M. J. Milgrew, M. Edwards, J. Hoon, J. F. Simons, D. Marran, J. W. Myers, J. F. Davidson, A. Branting, J. R. Nobile, B. P. Puc, D. Light, T. A. Clark, M. Huber, J. T. Branciforte, I. B. Stoner, S. E. Cawley, M. Lyons, Y. Fu, N. Homer, M. Sedova, X. Miao, B. Reed, et al., *Nature* **2011**, *475*, 348.
[17] L. Cohen, D. R. Walt, *Annu. Rev. Anal. Chem.* **2017**, *10*, 345.
[18] D. M. Rissin, C. W. Kan, T. G. Campbell, S. C. Howes, D. R. Fournier, L. Song, T. Piech, P. P. Patel, L. Chang, A. J. Rivnak, E. P. Ferrell, J. D. Randall, G. K. Provuncher, D. R. Walt, D. C. Duffy, *Nat. Biotechnol.* **2010**, *28*, 595.

[19] D. M. Rissin, D. R. Walt, *Nano Lett.* **2006**, *6*, 520.
[20] Quanterix, SP-X Imaging and Analysis SystemTM, https://www.quanterix.com/instruments/the-sp-x-imaging-and-analysis-system/, **2021**.
[21] C. Scandurra, K. Björkström, L. Sarcina, A. Imbriano, C. Di Franco, R. Österbacka, P. Bolella, G. Scamarcio, L. Torsi, E. Macchia, *Adv. Mater. Technol.* **2023**, 2201910.
[22] M. Jinek, K. Chylinski, I. Fonfara, M. Hauer, J. A. Doudna, E. Charpentier, *Science* **2012**, *337*, 816.
[23] V. L. Dao Thi, K. Herbst, K. Boerner, M. Meurer, L. P. M. Kremer, D. Kirrmaier, A. Freistaedter, D. Papagiannidis, C. Galmozzi, M. L. Stanifer, S. Boulant, S. Klein, P. Chlanda, D. Khalid, I. B. Miranda, P. Schnitzler, H. G. Kräusslich, M. Knop, S. Anders, *Sci. Transl. Med.* **2020**, *12*, eabc7075.
[24] M. Kaminski, O. Abudayyeh, J. S. Gootenberg, F. Zhang, J. Collins, *Nat. Biomed. Eng.* **2021**, *5*, 643.
[25] Abbott, Abbott ID NOW _Website, https://www.abbott.com/IDNOW.html?CID=OUS_OK)h, **2023**.
[26] W. Feng, A. M. Newbigging, J. Tao, Y. Cao, H. Peng, C. Le, J. Wu, B. Pang, J. Li, D. L. Tyrrell, H. Zhang, X. C. Le, *Chem. Sci.* **2021**, *12*, 4683.
[27] E. Macchia, K. Manoli, B. Holzer, C. Di Franco, M. Ghittorelli, F. Torricelli, D. Alberga, G. F. Mangiatordi, G. Palazzo, G. Scamarcio, L. Torsi, *Nat. Commun.* **2018**, *9*, 3223.
[28] E. Macchia, F. Torricelli, P. Bollella, L. Sarcina, A. Tricase, C. Di Franco, R. Österbacka, Z. M. Kovács-Vajna, G. Scamarcio, L. Torsi, *Chem. Rev.* **2022**, *122*, 4636.
[29] L. Sarcina, F. Viola, F. Modena, R. A. Picca, P. Bollella, C. Di Franco, N. Cioffi, M. Caironi, R. Österbacka, I. Esposito, G. Scamarcio, L. Torsi, F. Torricelli, E. Macchia, *Anal. Bioanal. Chem.* **2022**, *414*, 5657.
[30] E. Macchia, Z. M. Kovács-Vajna, D. Loconsole, L. Sarcina, M. Redolfi, M. Chironna, F. Torricelli, L. Torsi, *Sci. Adv.* **2022**, *8*, eabo0881.
[31] E. Macchia, L. Sarcina, C. Driescher, Z. Gounani, A. Tewari, R. Osterbacka, G. Palazzo, A. Tricase, Z. M. Kovacs Vajna, F. Viola, F. Modena, M. Caironi, F. Torricelli, I. Esposito, L. Torsi, *Adv. Electron. Mater.* **2021**, *7*, 2100304.
[32] E. Macchia, K. Manoli, C. Di Franco, R. A. Picca, R. Österbacka, G. Palazzo, F. Torricelli, G. Scamarcio, L. Torsi, *ACS Sens.* **2020**, *5*, 1822.
[33] E. Macchia, A. Tiwari, K. Manoli, B. Holzer, N. Ditaranto, R. A. Picca, N. Cioffi, C. Di Franco, G. Scamarcio, G. Palazzo, L. Torsi, *Chem. Mater.* **2019**, *31*, 6476.
[34] E. Macchia, K. Manoli, B. Holzer, C. Di Franco, R. A. Picca, N. Cioffi, G. Scamarcio, G. Palazzo, L. Torsi, *Anal. Bioanal. Chem.* **2019**, *411*, 4899.
[35] E. Macchia, L. Sarcina, R. A. Picca, K. Manoli, C. Di Franco, G. Scamarcio, L. Torsi, *Anal. Bioanal. Chem.* **2020**, *412*, 811.
[36] C. Scandurra, K. Björkström, L. Sarcina, A. Imbriano, C. Di Franco, R. Österbacka, P. Bolella, G. Scamarcio, L. Torsi, E. Macchia, *Adv. Mater. Technol.* **2023**, *8*, 2201910.
[37] K. Guo, S. Wustoni, A. Koklu, E. Díaz-Galicia, M. Moser, A. Hama, A. A. Alqahtani, A. N. Ahmad, F. S. Alhamlan, M. Shuaib, A. Pain, I. McCulloch, S. T. Arold, R. Grünberg, S. Inal, *Nat. Biomed. Eng.* **2021**, *5*, 666.
[38] L. Sarcina, E. Macchia, G. Loconsole, G. D'Attoma, P. Bollella, M. Catacchio, F. Leonetti, C. Di Franco, V. Elicio, G. Scamarcio, G. Palazzo, D. Boscia, P. Saldarelli, L. Torsi, *Adv. Sci.* **2022**, *9*, 2203900.
[39] E. Macchia, P. Romele, K. Manoli, M. Ghittorelli, M. Magliulo, Z. M. Kovács-Vajna, F. Torricelli, L. Torsi, *Flexible Print. Electron.* **2018**, *3*, 034002.
[40] Y. Bonnassieux, C. J. Brabec, Y. Cao, T. B. Carmichael, M. L. Chabinyc, K. T. Cheng, G. Cho, A. Chung, C. L. Cobb, A. Distler, H. J. Egelhaaf, G. Grau, X. Guo, G. Haghiashtiani, T. C. Huang, M. M. Hussain, B. Iniguez, T. M. Lee, L. Li, Y. Ma, D. Ma, M. C. McAlpine, T. N. Ng, R. Österbacka, S. N. Patel, J. Peng, H. Peng, J. Rivnay, L. Shao, D. Steingart, et al., *Flexible Print. Electron.* **2021**, *6*, 023001.
[41] F. Torricelli, D. Z. Adrahtas, F. Biscarini, A. Bonfiglio, C. A. Bortolotti, C. D. Frisbie, I. Mcculloch, E. Macchia, G. G. Malliaras, *Nat. Rev. Methods Prim.* **2021**, *1*, 66.
[42] J. Rivnay, S. Inal, A. Salleo, R. M. Owens, M. Berggren, G. G. Malliaras, *Nat. Rev. Mater.* **2018**, *3*, 17086.
[43] E. Macchia, L. De Caro, F. Torricelli, C. Di Franco, G. F. Mangiatordi, G. Scamarcio, L. Torsi, *Adv. Sci.* **2022**, *9*, 2104381.
[44] C. Di Franco, E. Macchia, L. Sarcina, N. Ditaranto, A. Khaliq, L. Torsi, G. Scamarcio, *Adv. Mater. Interfaces* **2023**, *10*, 2201829.
[45] National Cancer Institute, Surveillance, Epidemiology, and End Results Program, https://seer.cancer.gov, **2023**.
[46] J. Kleeff, M. Korc, M. Apte, C. La Vecchia, C. D. Johnson, A. V. Biankin, R. E. Neale, M. Tempero, D. A. Tuveson, R. H. Hruban, J. P. Neoptolemos, *Nat. Rev. Dis. Primers* **2016**, *2*, 16022.
[47] P. Rawla, T. Sunkara, V. Gaduputi, *World J. Oncol.* **2019**, *10*, 10.
[48] L. D. Wood, M. I. Canto, E. M. Jaffee, D. M. Simeone, *Gastroenterology* **2022**, *163*, 386.
[49] O. Basturk, S. Hong, L. Wood, N. Adsay, J. Albores-Saavedra, A. Biankin, L. Brosens, N. Fukushima, *Am. J. Surg. Pathol.* **2015**, *39*, 1730.
[50] I. D. Nagtegaal, R. D. Odze, D. Klimstra, V. Paradis, M. Rugge, P. Schirmacher, K. M. Washington, F. Carneiro, I. A. Cree, *Histopathology* **2020**, *76*, 182.
[51] O. Basturk, S.-M. Hong, L. D. Wood, N. V. Adsay, J. Albores-Saavedra, A. V. Biankin, L. A. A. Brosens, N. Fukushima, M. Goggins, R. H. Hruban, Y. Kato, D. S. Klimstra, G. Klöppel, A. Krasinskas, D. S. Longnecker, H. Matthaei, G. J. A. Offerhaus, M. Shimizu, K. Takaori, B. Terris, S. Yachida, I. Esposito, T. M. Furukawa, *Am. J. Surg. Pathol.* **2015**, *39*, 1730.
[52] M. W. Rosenbaum, M. Jones, J. C. Dudley, L. P. Le, A. J. Iafrate, M. B. Pitman, *Cancer Cytopathol.* **2017**, *125*, 41.
[53] A. D. Singhi, L. D. Wood, *Nat. Rev. Gastroenterol. Hepatol.* **2021**, *18*, 457.
[54] L. Haeberle, M. Schramm, W. Goering, L. Frohn, C. Driescher, W. Hartwig, H. K. Preissinger-Heinzel, T. Beyna, H. Neuhaus, K. Fuchs, V. Keitel-Anselmino, W. T. Knoefel, I. Esposito, *Sci. Rep.* **2021**, *11*, 2901.
[55] M. Del Chiaro, M. G. Besselink, L. Scholten, M. J. Bruno, D. L. Cahen, T. M. Gress, J. E. van Hooft, M. M. Lerch, J. Mayerle, T. Hackert, S. Satoi, A. Zerbi, D. Cunningham, C. De Angelis, M. Giovannini, E. de-Madaria, P. Hegyi, J. Rosendahl, H. Friess, R. Manfredi, P. Lévy, F. X. Real, A. Sauvanet, M. A. Hilal, G. Marchegiani, I. Esposito, P. Ghaneh, M. R. W. Engelbrecht, P. Fockens, N. C. M. van Huijgevoort, et al., *Gut* **2018**, *67*, 789.
[56] A. Facciorusso, V. Del Prete, M. Antonino, V. Buccino, S. Wani, *Gastrointest. Endosc.* **2020**, *92*, 1.
[57] S. Springer, D. Masica, M. Dal Molin, C. Douville, C. Thoburn, B. Afsari, *Sci. Transl. Med.* **2019**, *17*, 100.
[58] S. A. Safi, L. Haeberle, W. Goering, V. Keitel, G. Fluegen, N. Stoecklein, A. Rehders, W. T. Knoefel, I. Esposito, *Cancers* **2022**, *14*, 850.
[59] D. G. Rothwell, N. Smith, D. Morris, H. S. Leong, Y. Li, A. Hollebecque, M. Ayub, L. Carter, J. Antonello, L. Franklin, C. Miller, F. Blackhall, C. Dive, G. Brady, *Mol. Oncol.* **2016**, *10*, 566.
[60] G. Klöppel, O. Basturk, A. M. Schlitter, B. Konukiewitz, I. Esposito, *Semin. Diagn. Pathol.* **2014**, *31*, 452.
[61] J. M. Curry, K. J. Thompson, S. G. Rao, D. M. Besmer, A. M. Murphy, V. Z. Grdzelishvili, W. A. Ahrens, I. H. McKillop, D. Sindram, D. A. Iannitti, J. B. Martinie, P. Mukherjee, *J. Surg. Oncol.* **2013**, *107*, 713.
[62] K. Ohuchida, T. Ohtsuka, K. Mizumoto, M. Hashizume, M. Tanaka, *Gastrointest. Tumors* **2014**, *1*, 33.
[63] Z. He, H. Wu, Y. Jiao, J. Zheng, *Oncol. Lett.* **2015**, *9*, 793.
[64] The SiMBiT project, funded by European Union's Horizon 2020 research and innovation programme under grant agreement No.824946, https://simbit-h2020.eu/index.php.

[65] D. Blasi, F. Viola, F. Modena, A. Luukkonen, E. MacChia, R. A. Picca, Z. Gounani, A. Tewari, R. Österbacka, M. Caironi, Z. M. Kovacs Vajna, G. Scamarcio, F. Torricelli, L. Torsi, *J. Mater. Chem. C* **2020**, *8*, 15312.
[66] E. Genco, M. Fattori, P. J. A. Harpe, F. Modena, F. A. Viola, M. Caironi, M. Wheeler, G. Fichet, F. Torricelli, L. Sarcina, E. Macchia, L. Torsi, E. Cantatore, *IEEE Open J. Solid-State Circuits Soc.* **2022**, *2*, 193.
[67] L. Sarcina, L. Torsi, R. A. Picca, K. Manoli, E. Macchia, *Sensors* **2020**, *20*, 3678.
[68] R. Ehsani, F. Drabløs, *Cancer Inform.* **2020**, *19*, 1882255450.
[69] MathWorks – MATLAB & Simulink https://it.mathworks.com/?s_tid=gn_logo, **2023**.
[70] J. Mocak, A. M. Bond, S. Mitchell, G. Scollary, A. M. Bond, *Pure Appl. Chem.* **1997**, *69*, 297.
[71] G. P. R. Leardi, C. Melzi, Gruppodi Chemiometria, CAT (Chemometric Agile Tool) freely downloadable from http://gruppochemiometria.it/index.php/software, **2023**.